

Feasible Region: an Actuation-Aware Extension of the Support Region

Romeo Orsolino¹, Michele Focchi¹, Stéphane Caron², Gennaro Raiola¹, Victor Barasuol¹ and Claudio Semini¹

Abstract—In legged locomotion the support region is defined as the 2D horizontal convex area where the robot is able to support its own body weight in static conditions. Despite this definition, when the joint-torque limits (actuation limits) are hit, the robot can be unable to carry its own body weight, even when the projection of its Center of Mass (CoM) lies inside the support region. In this manuscript we overcome this inconsistency by defining the *Feasible Region*, a revisited support region that guarantees both global static stability of the robot and the existence of a set of joint torques that are able to sustain the body weight.

Thanks to the usage of an Iterative Projection (IP) algorithm, we show that the Feasible Region can be efficiently employed for *online* motion planning of loco-manipulation tasks for both humanoids and quadrupeds. Unlike the classical support region, the Feasible Region represents a *local* measure of the robots robustness to external disturbances and it must be recomputed at every configuration change. For this, we also propose a *global* extension of the Feasible Region that is configuration independent and only needs to be recomputed at every stance change.

Index Terms—static stability, motion planning, multi-contact legged locomotion, humanoids and quadrupeds.

SUPPLEMENTARY MATERIAL

- Video of simulation and experimental results: https://youtu.be/nmd_8jxtVbU
- Open-source python package: <https://github.com/orsoromeo/jet-leg>. Inside jet-leg/figures_code the source code used for the generation of Figs. 6, 8 and 9 can be found.

I. INTRODUCTION

The support polygon, defined as the convex hull of the contact points on a flat terrain, represents the first and most straightforward mathematical tool that has been employed for assessing the stability of legged robots. The distances between the edges of the support polygon and the considered ground reference point (*e.g.* the Center of Mass (CoM) projection \mathbf{c}_{xy} first, the Zero-tilting Moment Point (ZMP) \mathbf{z} [1] later and the Instantaneous Capture Point (ICP) ξ [2] more recently) are used in various criteria for the evaluation of the robot's robustness in static and dynamic gaits [3], [4].

Because of their restriction to coplanar contacts, the ground reference points have been extended to complex geometry

This work was supported by Istituto Italiano di Tecnologia.

¹Department of Advanced Robotics, Istituto Italiano di Tecnologia, Genova, Italy. email: {romeo.orsolino, michele.focchi, gennaro.raiola, claudio.semini} @iit.it

²Laboratoire d'Informatique, de Robotique et de Microélectronique de Montpellier (LIRMM), CNRS-University of Montpellier, Montpellier, France. email: stephane.caron@lirmm.fr

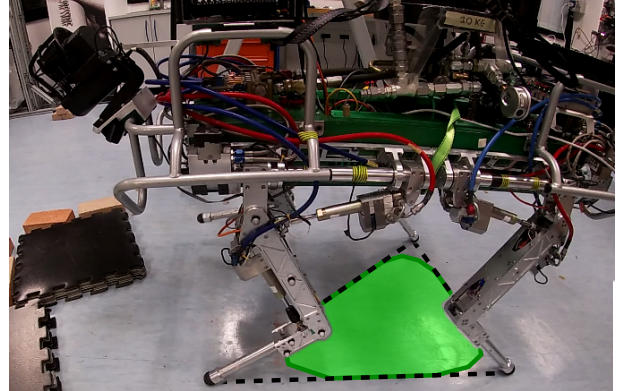


Fig. 1: HyQ robot walk with overlaid classical support region (dashed line) and local Feasible Region (green).

environments in different ways using nonlinear models, higher dimensional model representations or different spaces [5], [6], [7]. Wrench reference points (*i.e.* CoM linear and angular momentum rates), in particular, thanks to the accurate and compact description given by the *centroidal dynamics* [8], have received special attention in the domain of multi-contact locomotion planning because of their suitability for non-coplanar contact points and dynamic gaits. In this case the Contact Wrench Cone (CWC) can be seen as the wrench-space equivalent of the support polygon [9], [10]. However, none of the above mentioned strategies for the assessment of the robots stability attempts to include in the analysis the constraints imposed by, for example, the joint-torque limits (actuation limits) or the joint-kinematic limits of the robot. Such feasibility constraints are indeed usually only considered at the controller level [11]. Therefore, these strategies work well only under the assumption that the joint limits do not affect the locomotion capabilities of the legged robots. However, there exist situations where the complexity of the environment forces the robot to explore configurations that are close to its limits.

Joints' position and speed limits have been mapped to the task space for motion planning purposes through machine learning [12], [13] or through convex formulations of the dynamic equation of motion that can be efficiently solved as a Linear Program (LP) in multi-contact scenarios [14], [15].

The Actuation Wrench Polytope (AWP) and the Feasible Wrench Polytope (FWP) that have been described in our previous work [16], can be considered as a first attempt to increase the descriptiveness of the Contact Wrench Cone (CWC) by incorporating actuation limits. Just as the CWC,

the AWP and the FWP are valid for arbitrary contacts (not limited to flat terrains) and for dynamic motions with non-zero linear and angular momentum rates.

The computation time of six-dimensional bounded polytopes (AWP and FWP) increases considerably with respect to the case where only six-dimensional convex cones are involved¹ (*e.g.* CWC). In the case of a quadruped robot, for example, the FWP constraints can only be computed at about 10 Hz in a triple stance phase and about 3 Hz during a quadruple stance phase[16]. Such computational performances allow *online* motion planning to be achieved only under the assumption that the robot's configuration is not too far from the nominal configuration used to obtain the FWP limits. These restrictions, imposed by computational performances of modern processors, limit the effectiveness of wrench-based actuation-aware online planning.

The Iterative Projection (IP) algorithm introduced by Bretl *et al.* [17] can be used to overcome these limitations and project joint-space torque limits to a 2D dimensional space at rates that are, at least, 20 times faster than the ones obtained for 6D wrench polytopes.

The approach presented in this manuscript introduces the concept of *actuation region* and *feasible region* as two-dimensional counterparts of the AWP and FWP respectively. These regions are the projections of the AWP and FWP in the Cartesian (x, y) space orthogonal to gravity, obtained by assuming that gravity is the only external force acting on the robot and inertial accelerations are negligible. This quasi-static assumption enables the direct mapping from joint-torques to task space by means of a modified version of the IP algorithm, as originally proposed by Bretl *et al.* [17]. This allows us to check the feasibility margin with respect to friction-cone and joint-torque constraints at a frequency of, at least, 66 Hz for a triple support phase and 50 Hz for a quadruple stance phase of a quadruped. This implies that the robot is able to consider joint-torque limits in static conditions 20 times faster than the case where wrench polytopes are used. Despite the connections to our previous work, in this manuscript we develop a whole new strategy for the online planning of statically stable legged locomotion on arbitrary terrains. For this reason, this manuscript should not then be considered as an extended version of [16].

As later explained in Sec. III, the combination of wrench polytopes with the IP algorithm, enables the concurrent *online* optimization of actuation-aware CoM trajectories and foothold positions in rough terrains.

Besides that, the *actuation* and *feasible* regions can be easily represented in 2D, thus representing an *intuitive* aid for motion planning. This allows us to give a clear and *simple* answer to legitimate questions like: how does the step length change with the increase of the robot's mass? And also: which is the height of the highest step that a robot can step on given its maximal joint torque/force capabilities?

¹Convex cones hold the convenient property that their Minkowsky sum corresponds to their convex hull, thus making the computation of the CWC considerably faster than the FWP computation (see Appendix VII-B).

A. Contributions

In this manuscript we attempt to give an answer to the above questions in the following way:

- 1) We introduce a modified version of the IP algorithm initially proposed in [17], adapted to take into account joint-torque limits (*i.e.* *actuation limits*) of legged robots in the form of wrench (or force) polytope constraints;
- 2) We introduce the concept of *local* and *global* feasible regions and we discuss their properties. These 2D areas provide an *intuitive* yet powerful understanding of the relation between the task-space locomotion capabilities of a robot and its joint-space actuation limits;
- 3) We employ the proposed feasible region to formulate a motion planning algorithm for legged robots, able to optimize *online* the CoM trajectories and foothold locations on arbitrary terrains for predefined step sequences and timings (predefined by the duration of each gait's phase);
- 4) We report the results of hardware experiments where the online motion planner adapts the footstep locations and the trajectory of the robot's CoM to the geometry of the terrain.

B. Outline

The two core building blocks of the work developed in this manuscript are the wrench (or *force*) polytopes and the IP algorithm which are briefly recalled in Sec. II. Using the described elements we formulate the *local actuation region* \mathcal{Y}_a and the *local feasible regions* \mathcal{Y}_{fa} in Sec. III. In Section IV we then define the *global actuation region* and the *global feasible regions*, two 2D polygons that overcome the local restriction of \mathcal{Y}_a and \mathcal{Y}_{fa} . The latter, in particular can be seen as a revisited definition of the well known *support region*. Section IV-B introduces the possibility of computing 3D feasible volumes that can be used to guarantee that also the height of the robot's CoM lies within the set of feasible friction- and actuation-consistent configurations.

Section V presents examples of how the feasible region can be employed to achieve online planning CoM and feet trajectories on arbitrary terrains using the height map provided by the robot's exteroceptive sensors. Simulations on the humanoid robots HRP-4 and JRVC-1 and experimental results on the HyQ quadruped robot (see Fig. 1) are finally presented in Sec. VI. Section VII draws final conclusions regarding the concepts presented in this manuscript and anticipates possible future developments.

II. BACKGROUND

A. Wrench Polytopes for Fixed Base Systems

Actuator force/torque limits and their consequences on the overall performances in the task space have been analyzed for decades in the field on mechanical industrial manipulators [18], [19], [20] and, more recently on cable driven parallel robots [21] and robotics hands [22].

Wrench ellipsoids (or hyperellipsoids) have been identified as useful tools to assess the control authority at the end-effector of serial mechanical chains. However, they represent a *qualitative* metric and they do not hold any information relative to the

absolute magnitude of the wrench that a mechanical chain can exert. They can be obtained as a consequence of the kinetic energy theorem (or work-energy theorem) that states that the work done by all forces acting on a particle equals the rate of change in the particle's kinetic energy [23, p. 148]. This leads to the following:

$$\tau = \mathbf{J}(\mathbf{q})^T \mathbf{w} \quad (1)$$

which represents a static relationship between the generalized task-space wrenches $\mathbf{w} \in \mathbb{R}^m$ and the generalized joint-space forces $\tau \in \mathbb{R}^n$. The matrix $\mathbf{J}(\mathbf{q}) \in \mathbb{R}^{m \times n}$ is the end-effector Jacobian. If we consider (1) in combination with a unit hypersphere \mathcal{S}_τ in the joint torque space:

$$\mathcal{S}_\tau = \left\{ \tau \in \mathbb{R}^n \mid \tau^T \tau \leq 1 \right\} \quad (2)$$

we can then obtain a new set (the wrench ellipsoid) \mathcal{E}_w that describes how \mathcal{S}_τ is mapped into the task-space:

$$\mathcal{E}_w = \left\{ \mathbf{w} \in \mathbb{R}^m \mid \mathbf{w}^T \mathbf{J} \mathbf{J}^T \mathbf{w} \leq 1 \right\} \quad (3)$$

By definition, the force ellipsoid \mathcal{E}_w represents the pre-image of the unit hypersphere \mathcal{S}_τ in the joint space under the mapping given by $\mathbf{J}(\mathbf{q})^T$. The lengths of the semidiameters of \mathcal{E}_w are square root inverses of the singular values of $\mathbf{J}(\mathbf{q})$ [24, p.285]. The ratio between the greatest and the smallest eigenvalue of $\mathbf{J}(\mathbf{q})$ is, therefore, used as a measure of anisotropy of the ellipsoid and of the force amplification properties of the mechanical chain.

In a similar fashion, further exploiting (1), we can then also analyze the pre-image of the joint-torque hypercube \mathcal{Z}_τ , *i.e.* the set of all joint torques τ comprised within the manipulator's actuator limits:

$$\mathcal{Z}_\tau = \left\{ \tau \in \mathbb{R}^n \mid -\tau^{lim} \leq \tau \leq \tau^{lim} \right\} \quad (4)$$

The vector $\tau^{lim} \in \mathbb{R}^n$ contains in its elements the hardware dependent lower and upper bounds of the values that limit the generalized joint torque vector τ . The hypercube \mathcal{Z}_τ can therefore be seen also as a system of $2n$ linear inequalities that constrain joint torques [20] (see Fig. 2). The notation used in (4) assumes symmetric joint torques limits which is usually the case for the most common modern electric actuators; \mathcal{Z}_τ is in this case a zonotope centered at the origin (see Appendix VII-A). However, in the case of actuators with asymmetric joint-torque limits (*e.g.* for velocity dependent torque limits as in the case of hydraulic actuators with different chambers' volume or also for configuration-dependent torque limits as in the case of linear actuators with variable lever-arm of the HyQ robot) this notation can be updated to include such scenario without loss of the properties that are going to be described in the following sections. The hypercube \mathcal{Z}_τ will still represent a zonotope but its center will not correspond to the origin of joint-torque space.

The task-space wrench polytope \mathcal{P}_w , pre-image of \mathcal{Z}_τ , can be written as follows (also see Fig. 2):

$$\mathcal{P}_w = \left\{ \mathbf{w} \in \mathbb{R}^m \mid -\tau^{lim} \leq \mathbf{J}(\mathbf{q})^T \mathbf{w} \leq \tau^{lim} \right\} \quad (5)$$

While the force ellipsoid \mathcal{E}_w can be used as a qualitative metric of the robot's force amplification capabilities, the wrench

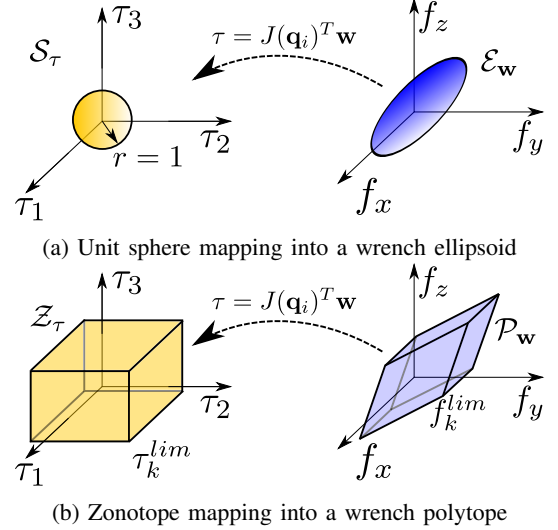


Fig. 2: The mapping between joint-space torques and the task-space forces at the end-effector. In this example, the dimension of joint-torque space $\dim(\mathcal{Z}_\tau) = \dim(\mathcal{S}_\tau) = n = 3$ is equal to the dimension of the manifold of the contact forces $\dim(\mathcal{P}_w) = \dim(\mathcal{E}_w) = m = 3$. The index $i = 0, \dots, n_l$ represents the limb's index while $k = 0, \dots, 2^n$ represents the vertices' index.

wrench polytope \mathcal{P}_w also includes quantitative informations about the maximum and minimum amplitude of the wrench that the robot can perform at the end-effector.

Wrench ellipsoids and wrench polytopes have been originally introduced for fixed-base non-redundant serial mechanical chains with $m = n$ where n is the number of actuated joints (dimension of generalized coordinates) and m is the dimension of the end-effector force (or, equivalently, the degree of constraint at the contact). In such cases the Jacobian matrix $\mathbf{J}(\mathbf{q})$ is thus squared and, except for singular configurations, its transpose \mathbf{J}^T can be inverted to obtain the \mathcal{V} -representation of the wrench polytope \mathcal{P}_w :

$$\mathbf{w}^{lim} = \mathbf{J}(\mathbf{q})^{-T} \tau^{lim} \quad (6)$$

where $\tau^{lim} \in \mathbb{R}^n$ is a vertex of \mathcal{Z}_τ and $\mathbf{w}^{lim} \in \mathbb{R}^m$ is a vertex of \mathcal{P}_w . This is a suitable condition in which a one-to-one relation between joint-space torques and task-space wrenches exists. In the case of an arm with 3 Degree of Freedom (DoFs) ($n = 3$), for example, a violation of one joint-torque limit will correspond to a point on a facet of \mathcal{Z}_τ and also to another point on a facet of the task-space polytope \mathcal{P}_w . Similarly, a violation of two (or three) joint-torque limits will correspond to a point on an edge (or a vertex) of the \mathcal{Z}_τ and also to another point on an edge (or a vertex) of the task-space polytope \mathcal{P}_w . See Appendix VII-A for the definitions of facets, edges and vertices for $n > 3$.

For a more detailed explanation about the effect of gravity on force ellipsoids and on other possible definitions of wrench polytopes for fixed base systems in dynamic conditions please refer to [25], [20], [26].

B. Wrench Polytopes for Floating Base Systems

In this section we illustrate the procedure to compute the *dynamic wrench polytopes* \mathcal{A} *i.e.* the set of feasible contact wrenches that a tree-structured floating base robot can perform at its contact points with the environment while moving. For this, let us consider the Equation of Motion (EoM) of a floating-base robot²:

$$\mathbf{M}(\mathbf{q})\dot{\mathbf{s}} + \mathbf{C}(\mathbf{q}, \mathbf{s}) + \mathbf{g}(\mathbf{q}) = \mathbf{S}\boldsymbol{\tau} + \mathbf{T}(\mathbf{q})^T \mathbf{f} \quad (7)$$

where $\mathbf{q} = [\mathbf{q}_b^T \ \mathbf{q}_j^T]^T \in SE(3) \times \mathbb{R}^n$ is the vector of generalized coordinates of the floating-base system, composed of the pose of the floating base $\mathbf{q}_b \in SE(3)$ and of the coordinates $\mathbf{q}_j \in \mathbb{R}^n$ describing the positions of the n actuated joints. The vector $\mathbf{s} = [\nu_b^T \ \dot{\mathbf{q}}_j^T]^T \in \mathbb{R}^{6+n}$ is the vector of the generalized velocities, $\boldsymbol{\tau} \in \mathbb{R}^n$ is the vector of actuated joint torques while $\mathbf{C}(\mathbf{q}, \mathbf{s})$ and $\mathbf{g}(\mathbf{q}) \in \mathbb{R}^{6+n}$ are the centrifugal/Coriolis and gravity terms, respectively. The matrix $\mathbf{M}(\mathbf{q}) \in \mathbb{R}^{(n+6) \times (n+6)}$ is the joint-space inertia matrix, $\mathbf{S} \in \mathbb{R}^{(6+n) \times n}$ is the actuated-joint selector matrix and $\mathbf{f} \in \mathbb{R}^{mn_c}$ is the vector of contact forces³ that are mapped into joint torques through the stack of Jacobians $\mathbf{T}(\mathbf{q}) \in \mathbb{R}^{mn_c \times (6+n)}$. If we split (7) into its underactuated and actuated parts, we get:

$$\underbrace{\begin{bmatrix} \mathbf{M}_b & \mathbf{M}_{bj} \\ \mathbf{M}_{bj}^T & \mathbf{M}_j \end{bmatrix}}_{\mathbf{M}(\mathbf{q})} \underbrace{\begin{bmatrix} \dot{\mathbf{v}}_b \\ \ddot{\mathbf{q}}_j \end{bmatrix}}_{\dot{\mathbf{s}}} + \underbrace{\begin{bmatrix} \mathbf{c}_b \\ \mathbf{c}_j \end{bmatrix}}_{\mathbf{C}(\mathbf{q}, \mathbf{s})} + \underbrace{\begin{bmatrix} \mathbf{g}_b \\ \mathbf{g}_j \end{bmatrix}}_{\mathbf{g}(\mathbf{q})} = \underbrace{\begin{bmatrix} \mathbf{0}_{6 \times n} \\ \mathbf{I}_{n \times n} \end{bmatrix}}_{\mathbf{B}} \boldsymbol{\tau} + \underbrace{\begin{bmatrix} \mathbf{J}_b^T \\ \mathbf{J}_q^T \end{bmatrix}}_{\mathbf{T}(\mathbf{q})^T} \mathbf{f}. \quad (8)$$

By inspecting the actuated part (bottom line corresponding to n equations), that results from the concatenation of the equations of motions of all the branches, we see that $\mathbf{J}_q \in \mathbb{R}^{(mn_c) \times n}$ is block diagonal and it can map joint torques into contact forces for each leg *individually*:

$$\mathbf{J}_q = \text{diag}(\mathbf{J}(\mathbf{q}_1), \dots, \mathbf{J}(\mathbf{q}_{n_c})) \quad (9)$$

where $\mathbf{J}(\mathbf{q}_i)$ with $i = 1, \dots, n_c$ are the Jacobians of the limbs in contact with the ground. Omitting the first row of (7) is convenient because it avoids the coupling term \mathbf{J}_b and one wrench polytope can then be computed for each individual limb.

On a similar line as the dynamic manipulability polytope \mathcal{P}_w defined in [18], we can now define a quantity that we call *dynamic wrench polytope* \mathcal{A}_i for each individual i^{th} branch of the tree structured robot:

$$\mathcal{A}_i = \left\{ \mathbf{f}_i \in \mathbb{R}^m \mid \exists \boldsymbol{\tau}_i \in \mathbb{R}^{n_i} \text{ s.t. } \mathbf{M}_{bi}^T \dot{\mathbf{v}}_b + \mathbf{M}_i \ddot{\mathbf{q}}_i + \mathbf{c}(\mathbf{q}_i, \dot{\mathbf{q}}_i) + \mathbf{g}(\mathbf{q}_i) = \boldsymbol{\tau}_i + \mathbf{J}(\mathbf{q}_i)^T \mathbf{f}_i, \quad -\boldsymbol{\tau}_i^{\text{lim}} \leq \boldsymbol{\tau}_i \leq \boldsymbol{\tau}_i^{\text{lim}} \right\} \quad (10)$$

where $i = 1, \dots, n_c$ is the contact index and n_c is the number of active contacts between the robot and the environment. The vectors $\mathbf{q}_i \in \mathbb{R}^{n_i}$ and $\boldsymbol{\tau}_i \in \mathbb{R}^{n_i}$ represent the joint-space

²We consider the floating-base robot composed by n_f branches (*e.g.* number of feet and/or hands), with n_c of them in contact with the environment and, each of them having a number n_l of actuated DoFs. Therefore, $n = \sum_{k=1}^{n_f} n_k$ represents the total number of actuated joints.

³Note that the Hydraulically actuated Quadruped (HyQ) robot has nearly point feet, henceforth we consider for this robot pure forces acting at contact points and no contact torque ($m = 3$).

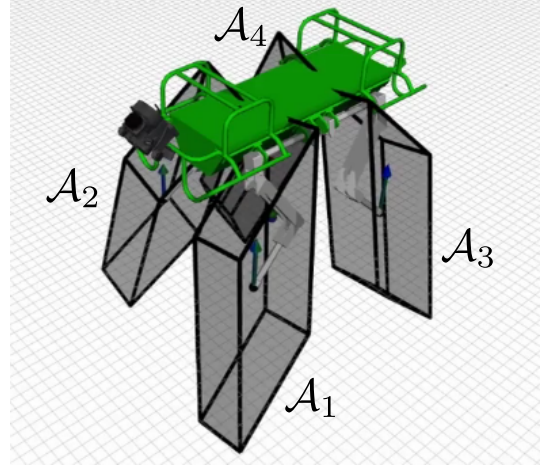


Fig. 3: Representation of the wrench polytopes \mathcal{A}_i on the feet of the HyQ robot ($i = 0, \dots, n_c$ is the leg index).

position and torque of only those joints that belong to the i^{th} limb while n_l represents the number of actuated DoFs of that limb. If $m = 3$ then the contact wrench $\mathbf{f}_i \in \mathbb{R}^m$ consists of pure forces while if $m = 6$ then a non-zero contact torque is also present. For a partial list of the main symbols employed in this paper and their meaning please refer to the Notation Section II-D.

In Fig. 3 an example of dynamic wrench polytope is drawn for the HyQ robot: each limb of this robot has three actuated DoFs ($n_l = 3$) and each foot can be approximated as a point contact ($m = 3$). \mathcal{A}_i is then a polytope of $2 \cdot 3 = 6$ facets and $2^3 = 8$ vertices (the mapping of a cube in the joint space).

(10) purposely omits the first line (six equations) of (8) referring to the unactuated floating base. This corresponds to neglecting the role of the base link as a coupling among the limbs of the tree-structured robot [27].

The advantage of computing separate individual wrench polytopes \mathcal{A}_i for each limb of the robot is that we can then treat each polytope as a wrench capability measure of the corresponding limb [28], [29].

As a final consideration, we can observe that in static conditions ($\dot{\mathbf{q}}_i = \ddot{\mathbf{q}}_i = 0$) (10) can be written as:

$$\mathcal{A}_i = \left\{ \mathbf{f}_i \in \mathbb{R}^m \mid \exists \boldsymbol{\tau}_i \in \mathbb{R}^{n_i} \text{ s.t. } \mathbf{g}(\mathbf{q}_i) = \boldsymbol{\tau}_i + \mathbf{J}(\mathbf{q}_i)^T \mathbf{f}_i, \quad -\boldsymbol{\tau}_i^{\text{lim}} \leq \boldsymbol{\tau}_i \leq \boldsymbol{\tau}_i^{\text{lim}} \right\} \quad (11)$$

The term $\mathbf{g}(\mathbf{q}_i)$ represents the effect of gravity acting on the individual limb $i = 0, \dots, n_c$. From a geometrical point of view $\mathbf{g}(\mathbf{q}_i)$ can also be seen as an offset term that translates the polytope \mathcal{A}_i in the same direction of the gravity vector, *i.e.* towards the negative side of the f_z direction of the wrench space defined by the axes $(f_x, f_y, f_z, \tau_x, \tau_y, \tau_z)$. For a predefined set of torque limits $\boldsymbol{\tau}_i^{\text{lim}}$ an increase in the legs mass and, as a consequence, a large offset term $\mathbf{g}(\mathbf{q}_i)$, will cause a decrease in the set of feasible positive contact forces.

C. The Iterative Projection Algorithm

The Iterative Projection (IP) algorithm is a method introduced by Bretl *et al.* [17] for the computation of support regions for articulated robots having multiple contacts with the environment in arbitrary locations, having arbitrary surface normals and friction coefficients. In [17], the support region is defined as *the horizontal cross section of the convex cylinder that represents the set of CoM positions at which contact forces exist that compensate for gravity without causing slip (for given foot placements with associated friction models)*.

The IP belongs to a family of cutting-plane methods [30] that allow to approximate a target convex set \mathcal{Y} up to a predefined tolerance value. The tuning of this tolerance allows to conveniently adjust the computational performance of the algorithm: it enables a rough but fast reconstruction of the target set for high tolerance values. On the other hand, it also enables a precise set reconstruction with longer solve times when the tolerance value is low.

Bretl *et al.* [17] have applied this algorithm to the field of legged locomotion with the goal to reconstruct the 2D friction-consistent support region \mathcal{Y}_f for the CoM in static equilibrium. This algorithm was also applied in derivative works to compute multi-contact ZMP support areas [31] or time-optimal trajectory retimings [32], [33]. In order to reduce the confusion with other similar regions that will be defined in the upcoming Sections, in the remainder of this manuscript the support region for the CoM in static equilibrium will be referred to simply as the *friction region*.

Algorithm 1 reports the procedure presented in [17]; one can notice that the algorithm recursively solves an Second Order Cone Program (SOCP) that maximizes the horizontal position of the CoM $\mathbf{c}_{xy} \in \mathbb{R}^2$ along the direction defined by the unit vector $\mathbf{a}_i \in \mathbb{R}^2$ (i being in this case the iteration index) while satisfying friction constraints.

Input: $\mathbf{c}_{xy}, \mathbf{p}_1, \dots, \mathbf{p}_{n_c}, \mathbf{n}_1, \dots, \mathbf{n}_{n_c}, \mu_1, \dots, \mu_{n_c}$;

Result: friction region \mathcal{Y}_f

initialization: \mathcal{Y}_{outer} and \mathcal{Y}_{inner} ;

while $area(\mathcal{Y}_{outer}) - area(\mathcal{Y}_{inner}) > \epsilon$ **do**

I) compute the edges of \mathcal{Y}_{inner} ;

II) pick the edge cutting off the largest fraction of \mathcal{Y}_{outer} ;

III) solve the SOCP:

$$\max_{\mathbf{c}_{xy}, \mathbf{f}} \mathbf{a}_i^T \mathbf{c}_{xy}$$

such that:

$$(III.a) \quad \mathbf{A}_1 \mathbf{f} + \mathbf{A}_2 \mathbf{c}_{xy} = \mathbf{t}$$

$$(III.b) \quad \|\mathbf{B}\mathbf{f}\|_2 \leq \mathbf{u}^T \mathbf{f}$$

IV) update the outer approximation \mathcal{Y}_{outer} ;

V) update the inner approximation \mathcal{Y}_{inner} ;

end

Algorithm 1: Bretl and Lall's Iterative projection algorithm

The algorithm considers the robot's CoM position \mathbf{c} , mass m , set of n_c contacts $\mathbf{p}_1, \dots, \mathbf{p}_{n_c} \in \mathbb{R}^3$ with corresponding surface normals $\mathbf{n}_1, \dots, \mathbf{n}_{n_c} \in \mathbb{R}^3$ and friction coefficients

$\mu_1, \dots, \mu_{n_c} \in \mathbb{R}$. The constraint (III.a) enforces the static equilibrium of the forces and moments acting on the robot due to gravity \mathbf{g} and contact forces $\mathbf{f} = [\mathbf{f}_1^T, \dots, \mathbf{f}_{n_c}^T]^T \in \mathbb{R}^{mn_c}$. The matrix $\mathbf{A}_1 \in \mathbb{R}^{6 \times mn_c}$ represents the grasp matrix of the set of point contacts⁴, $\mathbf{A}_2 \in \mathbb{R}^{6 \times 2}$ computes the x, y angular components $\tau_{\mathcal{O}}^x$ and $\tau_{\mathcal{O}}^y$ of the wrench generated by the action of gravity on the CoM \mathbf{c} of the robot expressed with respect to a fixed frame \mathcal{O} . (III.b) ensures that the friction cones constraint is satisfied. Note that the SOCP problem can be simplified to an LP by approximating regular friction cones by friction pyramids [34]. The matrix \mathbf{B} projects the contact forces $\mathbf{f}_i \in \mathbb{R}^m$ into the local contact frame and $\mathbf{u} \in \mathbb{R}^{mn_c}$ considers the limits of the friction cones in the local contact frames:

$$\begin{aligned} \mathbf{A}_1 &= [\bar{\mathbf{A}}_1 \quad \dots \quad \bar{\mathbf{A}}_{n_c}] \in \mathbb{R}^{6 \times mn_c}, \\ \mathbf{A}_2 &= \begin{bmatrix} 0 \\ -mg \times \mathbf{P}^T \end{bmatrix} \in \mathbb{R}^{6 \times 2}, \quad \mathbf{P} = \begin{bmatrix} 1 & 0 & 0 \\ 0 & 1 & 0 \end{bmatrix} \\ \mathbf{t} &= \begin{bmatrix} -mg \\ 0 \end{bmatrix}, \quad \mathbf{u} = \begin{bmatrix} \mu_1 \mathbf{n}_1 \\ \vdots \\ \mu_{n_c} \mathbf{n}_{n_c} \end{bmatrix} \end{aligned} \quad (12)$$

$$\mathbf{B} = \text{diag}(\mathbf{1}_3 - \mathbf{n}_1 \mathbf{n}_1^T, \dots, \mathbf{1}_3 - \mathbf{n}_{n_c} \mathbf{n}_{n_c}^T)$$

where $\mathbf{P} \in \mathbb{R}^{2 \times 3}$ is a selection matrix that selects the x, y components of the CoM and $\bar{\mathbf{A}}_i$ is a transformation matrix such that:

$$\bar{\mathbf{A}}_i = \begin{cases} \begin{bmatrix} \mathbf{1}_3 \\ [\mathbf{P}_i] \times \end{bmatrix} \in \mathbb{R}^{6 \times 3n_c} & \text{if } m = 3 \\ \begin{bmatrix} \mathbf{1}_3 & 0 \\ [\mathbf{P}_i] \times & \mathbf{1}_3 \end{bmatrix} \in \mathbb{R}^{6 \times 6n_c} & \text{if } m = 6 \end{cases} \quad (13)$$

With the above definitions, the *friction region* \mathcal{Y}_f is defined as the set of horizontal CoM coordinates $\mathbf{c}_{xy} \in \mathbb{R}^2$ for which there exists a set of contact forces that respects both static equilibrium and friction constraints:

$$\mathcal{Y}_f = \left\{ \mathbf{c}_{xy} \in \mathbb{R}^2 \mid \exists \mathbf{f} \in \mathbb{R}^{mn_c} \text{ s.t. } (\mathbf{c}_{xy}, \mathbf{f}) \in \mathcal{C} \right\} \quad (14)$$

where:

$$\begin{aligned} \mathcal{C} = \left\{ \mathbf{f} \in \mathbb{R}^{mn_c}, \quad \mathbf{c}_{xy} \in \mathbb{R}^2 \mid \mathbf{A}_1 \mathbf{f} + \mathbf{A}_2 \mathbf{c}_{xy} = \mathbf{t}, \right. \\ \left. \|\mathbf{B}\mathbf{f}\|_2 \leq \mathbf{u}^T \mathbf{f} \right\} \quad (15)$$

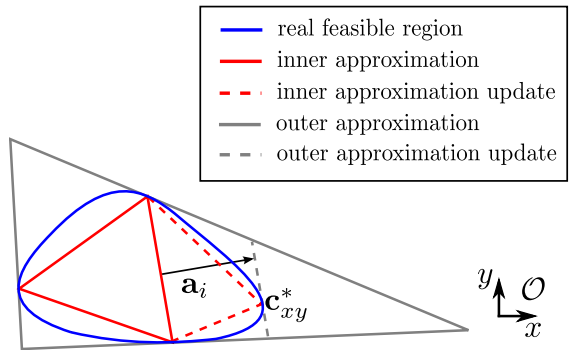


Fig. 4: Single step of Bretl and Lall's iterative projection algorithm

⁴ $[\cdot] \times$ represents the skew-symmetric operator associated to the cross product. $m = 6$ for generic contacts and $m = 3$ for point contacts.

Fig. 4 shows the process to compute one iteration of the IP algorithm reported in Alg. 1. As it can be seen in step III, the IP does not only maximize the horizontal CoM projection \mathbf{c}_{xy} along the direction $\mathbf{a}_i \in \mathbb{R}^2$, but it also finds a feasible set of contact forces \mathbf{f} that fulfills static equilibrium and friction cone constraints (constraints III.a and III.b).

Alg. 1 can also be regarded as a projection of the feasible set \mathcal{C} onto a two-dimensional region whose boundaries represent the limit torques $\tau_{\mathcal{O}}^x, \tau_{\mathcal{O}}^y$, that the robot can exert to balance the effect of gravity acting on its CoM. Exploiting the assumption that the only external force acting on the CoM is gravity we then get a one-to-one mapping between the torque components and the corresponding CoM (x, y) coordinates:

$$c_x = \frac{\tau_{\mathcal{O}}^y}{mg}, \quad c_y = -\frac{\tau_{\mathcal{O}}^x}{mg} \quad (16)$$

The friction region, as defined in (14), is a 2D convex set but it is not, in general, a linear set (*i.e.* it is not a polygon). The inner and outer approximations \mathcal{Y}_{inner} and \mathcal{Y}_{outer} used to estimate \mathcal{Y}_f are, however, always 2D polygons by construction. For this reason we will therefore refer to \mathcal{Y}_f in the rest of this paper with the term *friction region* rather than *friction polygon*.

Del Prete *et al.* [35] proposed a Revisited Incremental Projection (IPR) algorithm to test static equilibrium which is shown to be faster than the original IP formulation and than other possible techniques such as the Polytope Projection (PP). However the IPR approach is only suitable for convex cones and, therefore, does not fit well with the projection of bounded polytopes that we face in the next Section.

In the next Section we will see how we modified Alg. 1 in order to obtain a 2D set that does not only respect the static equilibrium and friction cone constraints, but it also respects the actuation capabilities of the system.

D. Notation

A partial list of the main symbols employed throughout this manuscript can be found in the following:

n	Number of actuated joints of the system
$\mathbf{c} \in \mathbb{R}^3$	Center of Mass (CoM) position
i	limb index
$\mathbf{p}_i \in \mathbb{R}^3$	End-effector position (hand or foot)
$\mathbf{f}_i \in \mathbb{R}^m$	wrench
$\boldsymbol{\tau} \in \mathbb{R}^n$	Joint-space torques
$\mathbf{q} \in SE(3) \times \mathbb{R}^n$	Point in robot's configuration manifold
$\dot{\mathbf{q}}_j \in \mathbb{R}^{6+n}$	Joint-space velocity
$\mathbf{q}_i \in \mathbb{R}^{n_i}$	Joints configuration of one single branch
$s \in \mathbb{R}^{6+n}$	Vector of generalized velocities
N	Num. of DoFs of the system
n_f	Branches of the tree-structured robot
n_c	Number of contacts
n_l	Actuated joints of one individual branch
n_i	Degrees of motions of the i^{th} joint.
m	dimension of the contact wrench

III. THE 2D LOCAL FEASIBLE REGION

Algorithm 1 can be extended in a straightforward manner to include also the static wrench polytope constraint that we already discussed in (11) in order to consider joint-torque limits besides the constraints imposed by the friction cones. The construction and analysis of the resulting 2D polygons, that we call *local feasible region*, will be the topic of the following Section.

A. Friction- and Actuation-Consistent Iterative Projection

In this Section we propose a variation of Alg. 1 to include also the static wrench polytope \mathcal{A}_i of every individual end-effector in contact with the environment. The resulting procedure can be found in Alg. 2.

Input:

$\mathbf{c}_{xy}, \mathbf{p}_1, \dots, \mathbf{p}_{n_c}, \mathbf{n}_1, \dots, \mathbf{n}_{n_c}, \mu_1, \dots, \mu_{n_c}, \mathbf{d}_1^{lim}, \dots, \mathbf{d}_{n_c}^{lim}, \mathbf{C}_1, \dots, \mathbf{C}_{n_c}$;

Result: local feasible region \mathcal{Y}_{fa}

initialization: \mathcal{Y}_{outer} and \mathcal{Y}_{inner} ;

while $\text{area}(\mathcal{Y}_{outer}) - \text{area}(\mathcal{Y}_{inner}) > \epsilon$ **do**

I) compute the edges of \mathcal{Y}_{inner} ;

II) pick the edge cutting off the largest fraction of \mathcal{Y}_{outer} ;

III) solve the SOCP:

$$\max_{\mathbf{c}_{xy}, \mathbf{f}} \mathbf{a}_i^T \mathbf{c}_{xy}$$

such that :

$$(III.a) \quad \mathbf{A}_1 \mathbf{f} + \mathbf{A}_2 \mathbf{c}_{xy} = \mathbf{t}$$

$$(III.b) \quad \|\mathbf{B}\mathbf{f}\|_2 \leq \mathbf{u}^T \mathbf{f}$$

$$(III.c) \quad \mathbf{C}\mathbf{f} \leq \mathbf{d}$$

IV) update the outer approximation \mathcal{Y}_{outer} ;

V) update the inner approximation \mathcal{Y}_{inner} ;

end

Algorithm 2: Actuation and Friction consistent IP algorithm (A_i, B, t, u are defined in Alg. 1)

We reformulate (11), representing the definition of wrench polytopes \mathcal{A}_i of the i^{th} limb in contact with the environment, as follows:

$$\mathcal{A}_i = \left\{ \mathbf{f}_i \in \mathbb{R}^m \mid \mathbf{C}_i \mathbf{f}_i = \mathbf{d}_i, -\tau_i^{lim} \leq \tau_i \leq \tau_i^{lim} \right\} \quad (17)$$

where:

$$\mathbf{C}_i = \mathbf{J}_i^T \in \mathbb{R}^{n_l \times m} \quad \text{and} \quad \mathbf{d}_i = \mathbf{g}(\mathbf{q}_i) - \boldsymbol{\tau}_i \in \mathbb{R}^{n_l} \quad (18)$$

where n_l is the number of actuated joints of the i^{th} limb. Differently from the original IP algorithm, we consider in this case the possibility of contact torques being applied at the end-effectors of the robot in contact with the environment; as a consequence we define each individual contact wrench $\mathbf{f}_i \in \mathbb{R}^m$ where $m = 3$ if the considered end-effector is perturbed by a pure force and $m = 6$ if, instead, also a contact torque component is given.

Considering the joint-space torque variable $\boldsymbol{\tau}_i$ (18) only depends on its minimum and maximum values τ_i^{lim} , we can then

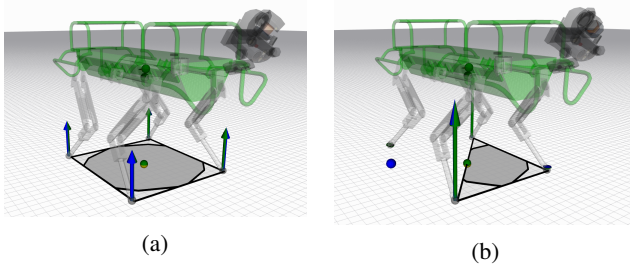


Fig. 5: Classical friction region (light gray) and feasible region (dark gray) in four-stance (a) and triple-stance (b) conditions.

further re-write (17) to explicitly highlight its dependency from τ_i^{lim} :

$$\mathcal{A}_i = \left\{ \mathbf{f}_i \in \mathbb{R}^m \mid \mathbf{C}_i \mathbf{f}_i \leq \mathbf{d}_i^{lim} \right\} \quad (19)$$

where:

$$\mathbf{d}_i^{lim} = \mathbf{g}(\mathbf{q}_i) - \tau_i^{lim} \quad (20)$$

(19) thus represents a compact notation for the static wrench polytope initially defined in (11). We will now exploit this notation to introduce the matrix $\mathbf{C} \in \mathbb{R}$ and the vector \mathbf{d} , result of the concatenation of all the matrices \mathbf{C}_i and vectors \mathbf{d}_i^{lim} of all the individual limbs in contact with the environment:

$$\begin{aligned} \mathbf{C} &= \text{diag}(\mathbf{C}_1, \dots, \mathbf{C}_{n_c}) \in \mathbb{R}^{d \times (m \cdot n_c)} \\ \mathbf{d} &= \begin{bmatrix} \mathbf{d}_1^{lim} \\ \vdots \\ \mathbf{d}_{n_c}^{lim} \end{bmatrix} \in \mathbb{R}^d \end{aligned} \quad (21)$$

where $d = \sum_{i=1}^{n_c} n_{l,i}$ is the sum of the number of joints of all the limbs in contact with the environment (e.g. $d = n$ if all the limbs of the robot are in contact). \mathbf{C} and \mathbf{d} can now be used to redefine the set of actuation-consistent forces/wrenches \mathcal{A} that satisfy all the individual wrench polytopes \mathcal{F}_i for $k = 1, \dots, n_c$:

$$\mathcal{A} = \left\{ \mathbf{f} \in \mathbb{R}^{mn_c}, \quad \mathbf{c}_{xy} \in \mathbb{R}^2 \mid \begin{array}{l} \mathbf{A}_1 \mathbf{f} + \mathbf{A}_2 \mathbf{c}_{xy} = \mathbf{t}, \\ \mathbf{C} \mathbf{f} \leq \mathbf{d} \end{array} \right\} \quad (22)$$

In analogy with (14), we can define a new set of actuation-consistent CoM positions called *local actuation region*:

$$\mathcal{Y}_a = \left\{ \mathbf{c}_{xy} \in \mathbb{R}^2 \mid \exists \mathbf{f} \in \mathbb{R}^{mn_c} \text{ s.t. } (\mathbf{c}_{xy}, \mathbf{f}) \in \mathcal{A} \right\} \quad (23)$$

As a further observation we notice that we are interested in computing the set of CoM positions \mathcal{Y}_{fa} that simultaneously satisfies both the friction and the actuation constraints (see Fig. 5). This can be obtained by considering the intersection of \mathcal{C} and \mathcal{A} :

$$\begin{aligned} \mathcal{C} \cap \mathcal{A} &= \left\{ \mathbf{f} \in \mathbb{R}^{mn_c}, \quad \mathbf{c}_{xy} \in \mathbb{R}^2 \mid \begin{array}{l} \mathbf{A}_1 \mathbf{f} + \mathbf{A}_2 \mathbf{c}_{xy} = \mathbf{t}, \\ \|\mathbf{B} \mathbf{f}\|_2 \leq \mathbf{u}^T \mathbf{f}, \quad \mathbf{C} \mathbf{f} \leq \mathbf{d} \end{array} \right\} \end{aligned} \quad (24)$$

Based on (24), the friction- and actuation-consistent region \mathcal{Y}_{fa} , called *local feasible region*, can be defined as:

$$\mathcal{Y}_{fa} = \left\{ \mathbf{c}_{xy} \in \mathbb{R}^2 \mid \exists \mathbf{f} \in \mathbb{R}^{mn_c} \text{ s.t. } (\mathbf{c}_{xy}, \mathbf{f}) \in \mathcal{C} \cap \mathcal{A} \right\} \quad (25)$$

In analogy with Alg. 1, Alg. 2 explains how \mathcal{Y}_{fa} can be computed efficiently.

Simultaneously imposing the inequality constraints (III.b) and (III.c) in Alg. 2 corresponds to performing an intersection of the friction cone \mathcal{C}_i with the polytopes \mathcal{A}_i of the corresponding contact point. This yields the set of all the contact forces that simultaneously respect both the friction cone constraints and the joint actuation limits of the j^{th} limb (see for example Fig. 3). Alg. 2, in practice, is equivalent to Alg. 1 with the only difference being the constraint (III.c) relative to the actuation limits.

Another variant of the same IP algorithm can be formulated to compute the *actuation region* \mathcal{Y}_a that only considers actuation constraints and no friction constraints. This can be obtained by simply removing the constraint (III.b) from the SOCP that is solved at the step III of Alg. 2. In this case, being (III.b) the only quadratic constraint, the maximization problem will then turn into an LP⁵.

Intermediate cases exist where some end-effector present unilateral contacts and other limbs present instead bilateral contacts (e.g. when a robot is climbing a ladder pushing with its feet and pulling with his hands). Such conditions can be captured by the presented IP modification by enforcing only the wrench polytope constraints on the bilateral contact points and by enforcing both friction pyramids and wrench polytopes on unilateral contacts. The wrench polytope \mathcal{A}_i , unlike the friction cones \mathcal{C}_i , is a configuration-dependent quantity and, as a consequence, its vertices will change whenever the robot changes its configuration. In order to highlight this property, we refer to the resulting friction- and actuation-consistent feasible region \mathcal{Y}_{fa} with the name of *local feasible region*. The term *local* points out the fact that the feasible region \mathcal{Y}_{fa} can be considered to be accurate only in a *neighborhood* of the current robot configuration. The distance between the current CoM projection \mathbf{c}_{xy} and the edges of \mathcal{Y}_{fa} can be considered as a combined measure of the instantaneous robustness of the robot's state with respect to the contacts' stability and joint-space torque limits. This distance can also be seen as a robustness measure against possible external loads being added on top of the robot that may move the robot's CoM even when its configuration does not change.

Friction cones (and the friction region \mathcal{Y}_f) only depend on the contact configuration and can thus be recomputed only at stance change. This is a convenient property to embed a notion of *contact stability* [34] in motion planning. Meanwhile, the wrench polytopes (and thus the feasible region \mathcal{Y}_{fa}), because of their *local validity* must be recomputed at every configuration change and thus make the motion planning formulation harder. However, this local validity is also the key element of the local actuation polytopes that, if properly exploited, can provide an insightful view on the relationship between robot configuration and maximal exerted force at the end-effectors. In what follows, we will drop the adjective *local* for the sake of compactness, however the actuation polytopes \mathcal{A}_i should always be regarded as instantaneous, configuration-

⁵The original problem could also become an LP by using a pyramid approximation of the friction cones

constraint	2D CoM space	6D CoM wrench
friction	friction/support reg. \mathcal{Y}_f	CWC
joint torques	actuation reg. \mathcal{Y}_a	AWP
friction & joint torques	feasible reg. \mathcal{Y}_{fa}	FWP

TABLE I: Analogies between 2D regions and 6D polytopes.

dependent quantities.

B. Relationship between 2D Feasible Regions and 6D Feasible Polytopes

To achieve a better understanding of feasible regions, it is useful to underline the parallel that exists between them and their 6D counterparts (see Tab. I). In particular, the friction region \mathcal{Y}_f can be seen as a particular case of the CWC criterion with only gravity acting on the CoM of the robot, in the same way also the local actuation region \mathcal{Y}_a can be seen as a specific case of the AWP and the feasible region \mathcal{Y}_{fa} can be seen as a specific case of the FWP [16].

For example is possible to show that a 2D region can be obtained from the relative 6D polytope (*e.g.* AWP or FWP) by slicing the latter in correspondence of the planes: $f_x = 0, f_y = 0, f_z = mg$ and $\tau_z = 0$. In this way only two DoFs are left which correspond to the τ_x and τ_y coordinates of the wrench space. The two-dimensional region that results from this slicing procedure can then be mapped through (16) into a set of feasible CoM coordinates \mathbf{c}_{xy} that corresponds to the relative region (*e.g.* \mathcal{Y}_a or \mathcal{Y}_{fa}).

Computing the AWP or the FWP, however, can be computationally demanding because of the high dimensionality and large amount of halfspaces and vertices. This is what motivated us to propose a variant of the IP algorithm that allows to directly map joint-torques constraints into 2D CoM limits. The computational improvements achieved by this choice are presented in the following Section.

C. Computation Time

The usage of the IP algorithm implies a significant speed up for the computation of the actuation region reaching average computation times in the order of milliseconds (see Fig. 6) which makes it suitable for online motion planning.

The solve time of the IP algorithm depends on the number of inequality constraints embedded in it (only friction constraints, only actuation constraints, or both). The most favorable scenario is when only friction cones are considered (red in Fig. 6): in the case of linearized friction cones with four facets per pyramid, the IP will present $4n_c$ inequalities. The least convenient scenario is instead when both friction pyramids and wrench polytope constraints are considered (blue in Fig. 6), in this case the IP will include $(4+2n_l)n_c$ inequalities (assuming that all the limbs in contact with the ground have same number of DoFs n_l and that the friction cones are linearized with 4 halfspaces). In the case of the HyQ quadruped this will result in 10 inequalities per foot contact; in the case of a humanoid robot with 6 DoFs per leg, instead, this will result in 16 inequalities per foot contact. Figure 7, for example, shows the friction region \mathcal{Y}_f (green) and the feasible region \mathcal{Y}_{fa} in

the case of the HRP-4 robot standing still in a configuration with non-coplanar contacts.

The last row of Fig. 6 shows that, even in such inconvenient condition where all contacts are subject to both friction and actuation constraints, the solve time is below 20ms in a four-stance configuration and below 15ms in a triple-stance configuration in 99.5% of the computations (blue histogram). This allows the efficient computation of the local feasible region at a frequency of, at least, 50 Hz in a four stance configuration and 66 Hz in a triple stance configuration of a quadruped robot⁶. These frequencies could be further increased by reducing the tolerance factor of the IP algorithm (the tolerance value we used was $10^{-6}m^2$).

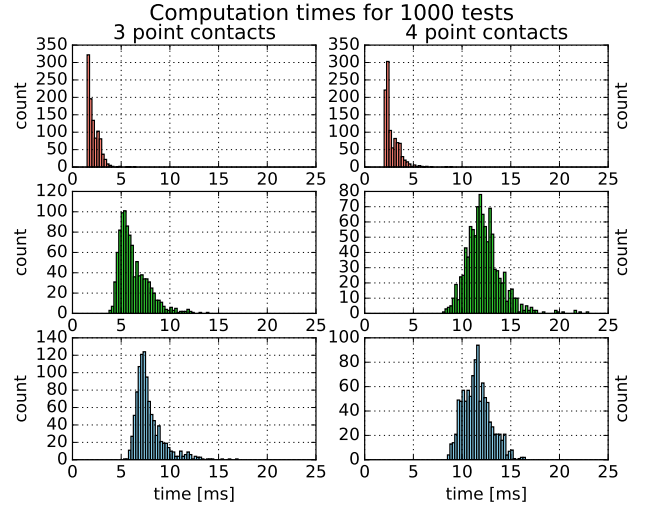


Fig. 6: Computation time of the IP algorithm with only friction cone constraints (red), only wrench polytope constraints (green) and both friction and actuation constraints (blue). These statistics were collected on a 4-core Intel(R) Core(TM) i5-4440 CPU @ 3.10 GHz processor.

⁶These computation times, as much as the other performances reported in this manuscript, have been achieved on a Intel(R) Core(TM) i5-4440 CPU @ 3.10GHz processor with 4 cores.

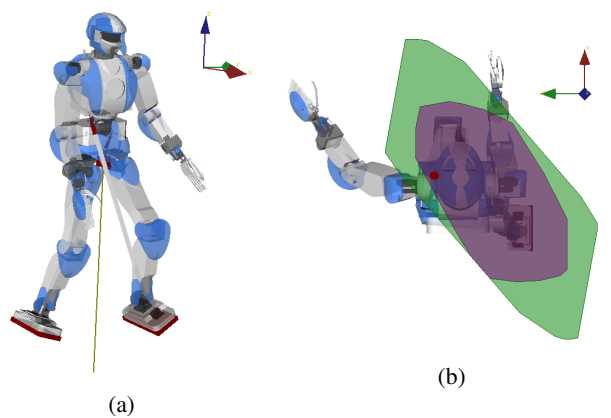


Fig. 7: Local feasible region (blue) and friction region (green) for the HRP-4 humanoid robot in a configuration with non-coplanar contacts.

D. Friction and Actuation-Consistent Whole-Body Controllers

Having the CoM inside the feasible region \mathcal{Y}_{fa} ensures the existence of a feasible set of contact forces that satisfy the wrench polytope constraints and the friction cone constraints. However, we still do not know the exact value of the forces corresponding to this feasible solution. From a control point of view, one should therefore develop a whole-body controller capable of computing these complementary forces.

On the other hand, if the CoM projection lies *outside* of \mathcal{Y}_{fa} , we can conclude that either the friction constraints or the joint-torques limits (or both) will be violated for that specific state of the robot.

Therefore, the proposed feasible region \mathcal{Y}_{fa} can also play a role in the field of benchmarking the performances of whole-body controllers (to make sure that they can still find a feasible solution when the CoM projection \mathbf{c}_{xy} lies inside \mathcal{Y}_{fa} or on the edge of \mathcal{Y}_{fa}).

Besides this, the friction-and-actuation consistent area \mathcal{Y}_{fa} does not suffer from limitations related to specific robot morphologies or specific terrains (*e.g.* flat terrains). As a consequence the friction-and-actuation consistent area \mathcal{Y}_{fa} can be employed for motion planning of legged robots on rough and complex terrains, where classical simplified models fail because the joint-torque limits affect more and more the robot's navigation capabilities.

E. Comparison of Local Feasible Regions

Fig. 8 reports various tests of computation of feasible 2D areas for different loads applied on the CoM of the robot. This is analogous to the computation of feasible regions for different percentages of torque limits while keeping the load on the robot fixed. The blue dashed lines represent the classical friction region \mathcal{Y}_f as defined by Bretl *et al.* [17].

Figs. 8a and 8c depict the *feasible regions* \mathcal{Y}_{fa} for the HyQ robot with four and three coplanar stance feet. Figs. 8b and 8d, instead, depict the *actuation regions* \mathcal{Y}_a in the same configurations with four and three coplanar stance feet. Such actuation consistent areas \mathcal{Y}_a alone are not directly applicable in the field of legged locomotion where robots typically make and break contacts using their feet and have therefore no possibility to grasp the terrain. Feasible regions \mathcal{Y}_{fa} should be used instead since they include the friction constraints that also naturally encode the unilaterality constraint. Actuation-consistent regions \mathcal{Y}_a however, can be useful in other fields of robotics such as manipulation or whenever a robot has bilateral contacts with the ground as in the case of climbing robots with magnetic grippers [36] or in the case of heavy-duty walking machines with predefined footstep locations such as the robots of the TITAN series [37]. As visible in Figs. 8b and 8d the robot's CoM might lean outside of the classical friction region \mathcal{Y}_f (dashed blue line) depending on the magnitude of the load acting on it: this is a typical condition in which one of the contacts is meant to *pull* the ground to maintain equilibrium. As a final consideration, comparing the figures related to the same number of stance feet (Fig. 8d compared with 8c and Fig. 8b compared with 8a) one can see that the feasible region \mathcal{Y}_{fa} cannot be obtained by simple intersection of the friction region

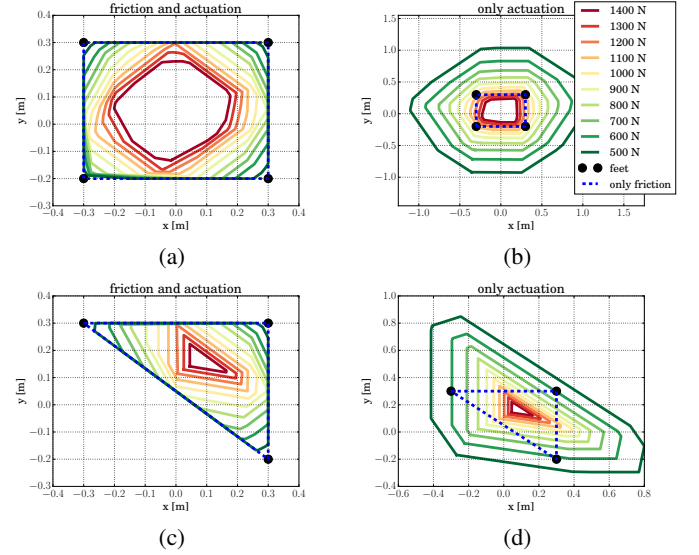


Fig. 8: Relation between the load acting on the CoM of the robot (in N) and the shape of the local feasible region. We can see that the heavier the load, the smaller the area of the feasible regions. The black points represent the stance feet positions of the HyQ quadruped during a four and triple support phases; the dashed blue lines represent the feasible region obtained by consideration of friction constraints only. The local feasible regions are computed in four possible scenarios:

- (a) 4 stance feet & friction and actuation constraints;
- (b) 4 stance feet & actuation constraints (no unilaterality);
- (c) 3 stance feet & friction and actuation constraints;
- (d) 3 stance feet & actuation constraints (no unilaterality);

\mathcal{Y}_f and the actuation region \mathcal{Y}_a . Although this approximation might be accurate under specific conditions, in general the intersection and projection operators do not commute [30]. Let us consider \mathcal{C} to be the set of contact forces and CoM positions \mathbf{c}_{xy} that respect static equilibrium and friction constraints (see (15)); let us then also consider \mathcal{A} defined as the set of contact forces and horizontal CoM positions \mathbf{c}_{xy} that respect all static equilibrium, wrench polytopes and friction cones constraints (see (19)). The *friction region* [17] can then be defined compactly as:

$$\mathcal{Y}_f = IP(\mathcal{C}), \quad (26)$$

the *local actuation region* as:

$$\mathcal{Y}_a = IP(\mathcal{A}) \quad (27)$$

and the (actuation- and friction-consistent) *local feasible region* as:

$$\mathcal{Y}_{fa} = IP(\mathcal{C} \cap \mathcal{A}) \quad (28)$$

where IP is the Iterative Projection operator. The projection and intersection are non-commutative operators and, in particular, the following inclusion always holds:

$$\mathcal{Y}_{fa} \subseteq \mathcal{Y}_f \cap \mathcal{Y}_a \quad (29)$$

\mathcal{Y}_{fa} is therefore more conservative than the intersection of \mathcal{Y}_f and \mathcal{Y}_a . Intuitively, (29) might be explained by considering that there may exist CoM positions that, at same the time:

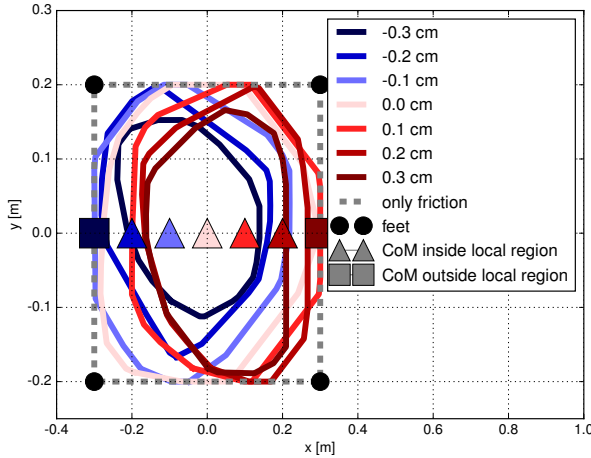


Fig. 9: Local actuation areas for the same foothold positions and for different CoM positions along the same segment. The triangular markers represent those CoM positions that do not belong to their correspondent local feasible region. The squared markers, instead, represent the tested CoM positions that are inside their correspondent local feasible region.

- 1) provide feasible wrench solutions if the friction cones or wrench polytope constraints are considered *individually*;
- 2) provide unfeasible wrench solutions if the friction cones or wrench polytopes constraints are considered *simultaneously*;

However, the opposite is not possible and consequently \mathcal{Y}_{fa} has to lie inside the intersection of \mathcal{Y}_f and \mathcal{Y}_a as stated in (29).

IV. THE GLOBAL ACTUATION AND FEASIBLE REGIONS

In this Section we address the issues due to the configuration dependency of the local feasible region and propose a *global* extension that is not configuration dependent and only depends on joint-torque limits and the location of contact points.

Figure 9 shows the local feasible region computed for different CoM positions (along the same segment from $(0, -0.3)$ to $(0, +0.3)$) and for the same set of contact points. As previously anticipated, the local feasible regions \mathcal{Y}_{fa} change as a function of the robot's configuration while the friction region \mathcal{Y}_f (dashed blue line) is constant as it only depends on the stance locations and orientation.

By inspection of the resulting actuation areas \mathcal{Y}_a is evident that some of the CoM positions \mathbf{c}_{xy} used for their computation do not lie within their corresponding local actuation region; such points are marked with squared markers. This is a degenerate condition in which the set of feasible forces/wrenches (constrained by the wrench polytopes and thus, ultimately, depending on the limb Jacobians \mathbf{J}_i and on the torque limits τ_i^{lim}) are not able to withstand the weight of the robot lumped into the specified value of \mathbf{c}_{xy} . Those cases are therefore to be considered unfeasible, even if the area of the resulting local actuation region is not empty. Such degenerate areas might be useful in the unlikely cases where the CoM position \mathbf{c}_{xy}

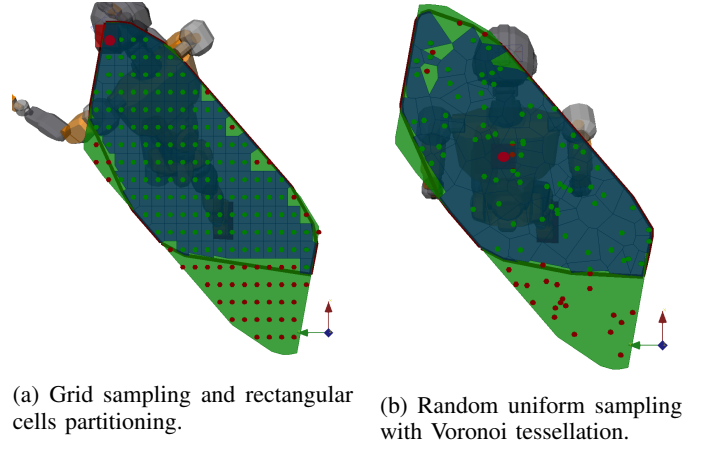


Fig. 10: Friction region (green) and global feasible region (blue) for the JVRC-1 humanoid robot.

changes without changing the robot configuration (*e.g.* when an external static load is added onto the trunk of the robot at a decentralized location).

Those points that, instead, do belong to their respective local actuation region are instead marked with triangular markers. By repeating the test shown in Fig. 9 along multiple directions and with multiple \mathbf{c}_{xy} positions (and, consequently different robot configurations) one can notice that the set of feasible CoM positions results in a convex set that we name *global actuation region* \mathcal{G}_a :

Definition 1: the static *global actuation region* \mathcal{G}_a is the set of all CoM coordinates $\mathbf{c}_{xy} \in \mathbb{R}^2$, lying on the plane orthogonal to the direction of gravity, where the robot is able to withstand its own weight considering its own joint-kinematic and joint-torque limits.

The definition above does not include the unilaterality of contact forces nor friction constraints; we thus define as follows a second global region that also considers such features (see Tab. II).

Definition 2: the static *global feasible region* \mathcal{G}_{fa} is the set of all CoM coordinates $\mathbf{c}_{xy} \in \mathbb{R}^2$, orthogonal to the direction of gravity, where the robot is able to withstand its own weight, considering its own kinematics, its joint-torque limits, the unilaterality of contact forces and the friction constraints.

The two areas \mathcal{G}_a and \mathcal{G}_{fa} , unlike their local counterparts \mathcal{Y}_a and \mathcal{Y}_{fa} , are *independent* from the robot configuration and they only depend on contact locations.

Figure 10 shows the global feasible area \mathcal{G}_{fa} (blue area) and the friction region \mathcal{Y}_f (green area) for the Japan Virtual Robotics Challenge (JVRC-1) humanoid robot [38]. The blue

constraint	2D CoM space	validity
friction	friction/support region \mathcal{Y}_f	global
joint-torques	actuation region \mathcal{Y}_a	local
friction & joint-torques	feasible region \mathcal{Y}_{fa}	local
joint-torques	actuation region \mathcal{G}_a	global
friction & joint-torques	feasible region \mathcal{G}_{fa}	global

TABLE II: Summary about the local/global validity of feasible regions.

region \mathcal{G}_{fa} in Fig. 10a was obtained by consecutively computing the local actuation areas over a two-dimensional grid of points with a predefined resolution. Considering that, by construction, the global feasible area \mathcal{G}_{fa} must be included inside the friction region \mathcal{Y}_f (green), grid points were only generated inside \mathcal{Y}_f .

The red (resp. green) dots in Fig. 10 correspond to those CoM locations that do not (resp. do) belong to their own local feasible region. For a green grid point, we intersect the local actuation region with a small rectangle of grid dimensions so as to enforce the fact that the local actuation region is only valid in a small neighborhood of the corresponding grid point. The global feasible region (dark green line) \mathcal{G}_{fa} is then obtained as the convex hull of all local blue regions. One can observe that some grid points that should be inside \mathcal{G}_{fa} are actually red because of numerical artifacts close to the boundaries.

The explained strategy yields the desired global actuation region \mathcal{G}_{fa} , however, the computation is not efficient (a new IP problem has to be solved at every grid point) and its accuracy depends on the predefined resolution of the grid map. We propose a more efficient strategy based on uniform random sampling and the use of Voronoi tessellation, as shown in Fig. 10b. The partition is generated starting from a uniform distribution of n sample points in a convex set (in this case inside \mathcal{Y}_f). Recall that using a uniform distribution to generate a Voronoi diagram minimizes the variance of the areas of each individual Voronoi cells. By intersecting local actuation regions with the Voronoi cell of their sample point, we can compute the same area \mathcal{G}_{fa} as previously, yet with a sample size that is less than half of the initial strategy.

A. Sequential Iterative Projection (SIP) Algorithm

In this Section we present an alternative to the previous sampling-based approaches for the computation of the global feasible region. This consists of a recursive solution of the IP algorithm presented in Section III-A (Alg. 2). The algorithm is based on the observation that, if the same set of contacts is kept, varying the robot configurations will result in one of the two following events:

- 1) \mathcal{Y}_{fa} degenerates to an empty area (either because the Jacobian matrix \mathbf{J}_i , used for the computation of \mathbf{C} in (21), becomes singular or because torque limits are exceeded);
- 2) \mathcal{Y}_{fa} has a positive area but the projection of the CoM is not inside it (as mentioned in Sec. IV).

Case 1) occurs most commonly when the robot's load increases beyond the maximum value allowed by the joint-torque limits. If, instead, the robot's mass is constant (no external loads and/or disturbances) then the event 2) usually occurs before event 1).

Based on this observation, starting from a default CoM position we update the robot's configuration while we move the CoM along a desired direction, represented by the unit vector $\mathbf{a} \in \mathbb{R}^2$, and sequentially recompute the instantaneous actuation region (using Alg. 2) until the distance between the

Input:

$\mathbf{c}, \mathbf{p}_1, \dots, \mathbf{p}_{n_c}, \mathbf{n}_1, \dots, \mathbf{n}_{n_c}, \mu_1, \dots, \mu_{n_c}, \mathbf{g}_1, \dots, \mathbf{g}_{n_c};$
 $\mathbf{J}_1, \dots, \mathbf{J}_{n_c}, \tau_1^{lim}, \dots, \tau_{n_c}^{lim};$

Result: vertex $\hat{\mathbf{c}}$ of the global feasible region \mathcal{G}_{fa} along the direction $\mathbf{a} \in \mathbb{R}^2$

Initialization: set the initial vertex guess $\hat{\mathbf{c}} \in \mathbb{R}^2$ equal to the default CoM (x, y) coordinates: $\hat{\mathbf{c}}_0 = P\mathbf{c}$;

Set $d = \infty$ and $\epsilon \rightarrow 0$;

while $d > \epsilon$ **do**

I) compute the contact points $\hat{\mathbf{p}}_1, \dots, \hat{\mathbf{p}}_{n_c}$ in the new CoM frame located in $\hat{\mathbf{c}}_i$;

II) solve inverse kinematics: $\mathbf{q} = IK(\hat{\mathbf{p}}_1, \dots, \hat{\mathbf{p}}_{n_c})$;

III) compute \mathbf{C} and \mathbf{d} as in (21) for the joint configuration \mathbf{q} ;

IV) $\mathcal{Y}_{fa} = IP(\mathbf{A}_1, \mathbf{A}_2, \mathbf{B}, \mathbf{u}, \mathbf{C}, \mathbf{d})$;

V) find the intersection $\mathbf{e} \in \mathbb{R}^2$ between the desired direction \mathbf{a} and the edges of \mathcal{Y}_{fa} ;

VI) $d = \|\mathbf{e} - \hat{\mathbf{c}}\|_2$;

VII) update the vertex $\hat{\mathbf{c}}$ towards \mathbf{e} :

$$\hat{\mathbf{c}}_{k+1} = \hat{\mathbf{c}}_k + \alpha(\mathbf{e} - \hat{\mathbf{c}}_k)$$

end

Algorithm 3: Sequential Iterative Projection (SIP) Algorithm

edges of \mathcal{Y}_{fa} and the CoM projection becomes smaller than the predefined acceptable tolerance ϵ (see Alg. 3).

Differently from the tests reported in Fig. 9 (where all the CoM were homogeneously distributed along one segment), in this case we increasingly update the new tested CoM position $\hat{\mathbf{c}}$ of a given gain α of the distance d between the current value of the CoM position and the intersection \mathbf{e} between the local region \mathcal{Y}_{fa} and the considered search direction:

$$d = \|\mathbf{e} - \hat{\mathbf{c}}\|_2 \quad (30)$$

With the usage of a suitable gain α , this allows the distance d to recursively converge to zero; whenever the distance becomes lower than the predefined tolerance ϵ the procedure is stopped and the latest CoM position $\hat{\mathbf{c}}$ is considered to be a vertex of the global feasible region \mathcal{G}_{fa} .

This strategy allows to efficiently find a vertex on the edge of the global feasible region by recursive computations of the IP algorithm. The strategy can then be repeated in multiple directions (see for example Fig. 11b) in order to reconstruct the entire global feasible region \mathcal{G}_{fa} or just a part of it in the region of most interest.

The Sequential Iterative Projection (SIP) algorithm can also be considered as a sequential linearization algorithm that recursively estimates the robustness of the considered CoM along a specific motion direction. It could be used, for instance, to estimate how far ahead in a specific direction the CoM may move without violating neither friction nor actuation constraints. Alternatively, a variant can be considered where, rather than testing different CoM positions and/or trunk orientations, different foot positions are tested. This might be interesting for example for foothold planning applications.

The underlying idea of the SIP algorithm (*i.e.* to sequentially change one quantity (CoM position, trunk orientation or feet

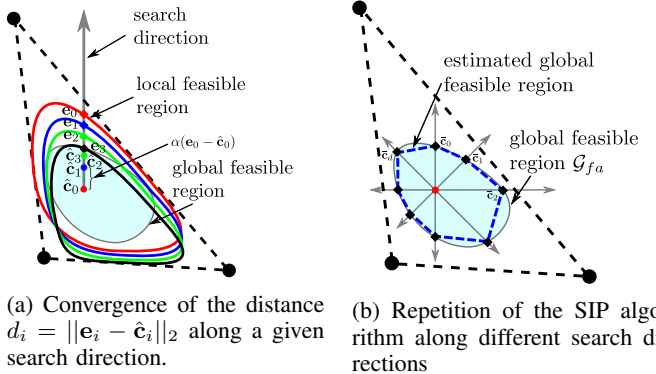


Fig. 11: Visual representation of the estimation of the global feasible region using the SIP algorithm.

positions) and to-recompute a new local area till when the convergence criterion is met) remains therefore valid.

The global feasible region \mathcal{G}_{fa} as defined so far is independent from the robot's (x, y) coordinates; however, it still depends on the robot's height and trunk orientation. In the next Section we will attempt to exploit the dependency of \mathcal{G}_{fa} from the robot's height (z coordinate) in order to estimate a 3D volume of friction- and actuation-consistent CoM positions.

B. 3D Global Feasible Volume

Fig. 12 depicts the JVRC-1 robot climbing a vertical ladder. In this case, we model the robot with unilateral contact constraints (intersection of friction cones and wrench polytopes) at the feet and bilateral contacts (only wrench polytopes and no friction cone constraints) at the hands. We then compute the friction region \mathcal{Y}_f using Alg. 1 setting infinite values of the friction coefficient on hand contacts. This yields as a result the whole horizontal plane as friction region. This is due to the fact that, because of the opposition of the contacts on the vertical ladder, the robot is able to exert any contact force, so it could ideally locate its CoM anywhere in the x, y plane (if kinematic limits are not considered).

The blue convex set in Fig. 12a is the global feasible region \mathcal{G}_{fa} . The blue 3D volume in Fig. 12b is the convex hull of multiple \mathcal{G}_{fa} computed at different robot heights. \mathcal{G}_{fa} can therefore be seen as a slice of the blue 3D volume in the direction orthogonal to gravity.

In the ladder climbing scenario, the robot-specific kinematics highly affect the climbing capabilities of the robot. This can be captured by the upper and lower bounds of the 3D feasible volume which, depending on the values of the torque limits, may be due to either of two following causes:

- 1) the area of the 2D global feasible region \mathcal{G}_{fa} converging to zero. This condition is due to the magnitude of the actuation limits which is too low to carry the body weight for that configuration;
- 2) the arms or legs' Jacobians reaching a kinematic singularity (*i.e.* point 1 in Section IV-A). This is due to a degeneration of the wrench polytopes, regardless the value of the actuation limits.

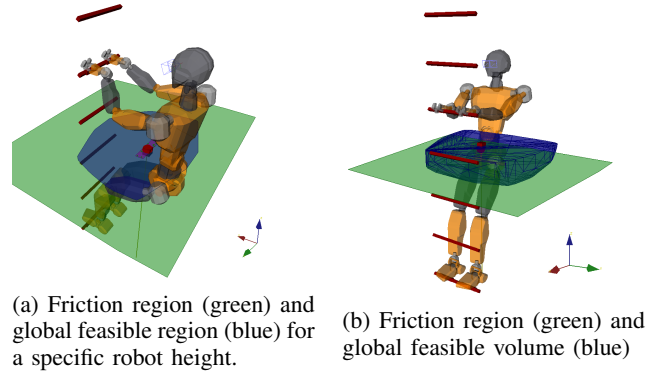


Fig. 12: JVRC-1 humanoid robot climbing a ladder.

The usage of 3D feasible volumes, such as the one shown in this picture, could overcome the typical limitation of static equilibrium approaches for which the CoM height c_z is unobservable (because parallel to gravity). Such 3D volumes could indeed enable the planning of friction- and actuation-consistent robot height trajectories (besides the planning of the coordinates orthogonal to gravity) at the price of larger computation times.

V. CENTER OF MASS AND FOOTHOLD PLANNING

In this Section we employ the concept of local feasible region \mathcal{Y}_{fa} introduced in Section III-A for the sample-based optimization of feasible footholds and CoM trajectories. Online replanning is achieved thanks to the computational efficiency of the local regions computation. The proposed strategy is valid for statically stable locomotion over complex terrain geometry.

The primary ingredient is the minimum distance r between the CoM projection $\mathbf{c}_{xy} = \mathbf{P}\mathbf{c}$ and the edges of the local feasible region. This can be found by solving the following LP:

$$\arg \max_r \quad \mathbf{a}_i^T \mathbf{c}_{xy} + \|\mathbf{a}_i\|_2 r \leq b_i, \quad i = 0, \dots, N_h \quad (31)$$

where N_h is the number of edges of \mathcal{Y}_{fa} , $\mathbf{a}_i \in \mathbb{R}^2$ is the normal to the i^{th} edge and $b_i \in \mathbb{R}$ is the known term. r is thus the radius of the largest ball centered in \mathbf{c}_{xy} and inscribed inside \mathcal{Y}_{fa} . and it can also be seen as a static instantaneous measure (*i.e.* a margin) of how far the robot is from slipping or from hitting one of joint-torque limits (actuation limits).

A. CoM planning strategy

As we only deal with CoM planning in this Section, we will assume the gait sequence, phase timings and step locations to be predefined. Since the feasible region, at the actual state, is restricted by the quasi-static assumption (an extension to the dynamic case with non-negligible CoM horizontal acceleration is part of future works) a quasi-static gait is a good template to test its applicability.

As the main hardware platform for our experiments is the quadruped robot HyQ, we will consider here a static quadrupedal gait called *crawl* [39]. In the crawl is divided

in two main phases called *swing phase* and *move-base phase*. During the swing phase, the robot does not move its trunk and only one foot at the time is allowed to lift-off from the ground and move to a new foothold while all the other three feet have to be in stance. During the move-base phase, instead, all four feet are in stance and the robot moves its trunk to a target location and orientation.

The most critical phase, in terms of stability and margin with respect to the joints torque limits, is this triple stance phase (*i.e.* the swing phase) because the robot's weight must be distributed only on three legs. The CoM is meant to move only during the four-stance phase, to enter the future support region which is opposite to the next swing leg. Therefore, after each touchdown, we re-plan a polynomial trajectory that links the actual CoM position with a new target inside the future support region. This enables us to completely unload the swing leg before liftoff and naturally distribute the weight onto the other three stance legs. In our previous work [39] we computed this target heuristically without any awareness of joint-torque limits. Specifically, we were computing the target point at a *hand-tuned* distance from the main diagonal of the support triangle, in order to *sufficiently* load the off-diagonal leg. However, this can be inaccurate in complex terrains, because:

- 1) the local friction region \mathcal{Y}_f coincides with the local feasible region \mathcal{Y}_{fa} only when every individual limb of the robot is able to carry the total body weight of the robot;
- 2) an increased load on the robot or an inconvenient robot configuration can further restrict the feasible region \mathcal{Y}_{fa} making it considerably smaller than the friction region.

Therefore, the heuristic target, since it is not formally taking these aspects into account, might fail in situations that are more demanding due to a complex terrain geometry. Conversely, using feasible regions to compute the location of the CoM target, allows us to select the target for the CoM that results in a statically stable robot configuration, in the case of: 1) a generic terrain shape (*i.e.* non coplanar feet, each one with different normal at the contact) 2) different loading conditions (because it considers the actuation limits of the robot).

Planning the target in a scaled region also allows us to increase the robustness against external disturbances and uncertainties, in accordance to the chosen scaling factor.

At the touch-down instant, we compute the *local* feasible region \mathcal{Y}_{fa} , considering as inputs the position of the three stance feet of the future support triangle (the feet sequence is predefined) and the corresponding normals n_i at the expected contact points. To evaluate Jacobians (necessary to map the actuation constraints into a set of admissible contact forces), we also provide the future CoM position predicted by the heuristics⁷ If the projection of the actual CoM $\mathbf{c}_{xy} = \mathbf{P}\mathbf{c}$ is inside \mathcal{Y}_{fa} , we then set the target CoM equal to the actual CoM $\mathbf{c} \in \mathbb{R}^3$. If it is, instead, outside the region \mathcal{Y}_{fa} , we set

⁷In the case of the global feasible region this is no longer necessary. However, since the computation time to obtain the global region is much higher than the time required to compute \mathcal{Y}_{fa} , for online re-planning, we stick to the instantaneous region. In future works we intend to embed the computation of the global feasible region in the online motion planner.

the target CoM equal to the point x^* on the boundary of the region (or of the scaled region if we want to provide a certain degree of robustness) that is closest to \mathbf{c}_{xy} . This allows us to minimize unwanted lateral/backward motions. To obtain the point x^* we solve the following QP program:

$$\mathbf{x}^* = \underset{\mathbf{x} \in \mathbb{R}^2}{\operatorname{argmin}} \|\mathbf{x} - \mathbf{P}\mathbf{c}\|^2 \quad (32)$$

$$\text{subject to: } \mathbf{A}\mathbf{x} \leq \mathbf{b} \quad (33)$$

where we minimize the Euclidean distance between a generic inner point x and the actual CoM c_{xy} . \mathbf{A} and \mathbf{b} matrix represent the half-space description of the polygon \mathcal{Y}_{fa} .

The CoM target is depicted as a yellow cube in Fig. 13 while the blue cube represents the heuristic target. In the same picture we show an image of the feasible region \mathcal{Y}_{fa} (light gray) and the scaled feasible region (dark gray) scaled by a factor of 0.8. The dashed triangle represents the friction region \mathcal{Y}_f ⁸. The scaling procedure can be defined as an affine transformation that preserves straight lines and parallelism relationships among the edges of the feasible region. The scaling can be done with respect to the Chebyshev center (*i.e.* the center of the largest ball inscribed in the feasible region) or with respect to the centroid. The former is more computationally expensive because it requires the solution of an LP; the latter is faster to compute because it can be found analytically as the average of all the vertices. The centroid can be considered as a good approximation of the Chebychev center whenever the feasible region presents good symmetry properties. Whenever the feasible region is not symmetric, however, the centroid might considerably differ from the Chebychev center thus resulting in a value of the robustness margin r lower than desired. In the case of the centroid, the vertices \hat{v} of the scaled region $\hat{\mathcal{Y}}_{fa}$ can be computed by scaling the vertices v of \mathcal{Y}_{fa} as: $\hat{v} = s(v - v_c) + v_c$ where v_c is their centroid and $s \in (0.0, 1.0]$ is the scaling factor.

As previously mentioned, notice that the feasibility margin defined here represents a method to verify whether there exists a set of admissible joint torques that can withstand the robot's weight for the considered configuration. In practice, however, depending on the implementation of the whole-body controller, one of the torque limits might be reached even when the margin r is still positive [16]. This is because, due to the force redundancy, the whole body controller can map the centroidal wrench onto the ground reaction forces in an infinity of ways. For example, for a certain mapping, a torque limit on a specific joint can be hit, but there might exist another solution where the load is redistributed on the other joints where that limit is not hit anymore. A positive margin in the feasible region, only tells us the existence of at least one solution where none of the torque limits are hit. The usage of an actuation-consistent whole-body controller that explicitly enforces torque constraints, (suitable implementations of such

⁸Note that just scaling the value of joint-torque limits (instead of the vertices of the feasible region) might not result in a conservative region. This is because some boundaries of the resulting feasible region could be determined by the friction region itself, thus reducing the joint-torque limits would not result in an increase of robustness with respect to those boundaries. For this reason, it is advisable to scale directly the vertices of the feasible region rather than joint-torque limits used to compute the feasible region.

controllers can be found, by instance, in [40], [41], [42]) it will find a non-torque-violating solution whenever there is one.

B. Foothold Planning

The foothold planning strategy that we present in this Section represents a sample-based strategy to improve the navigation capabilities of the HyQ quadruped robot on rough terrains. Our strategy employs the map provided by the perception module and seeks among the terrain samples the foot location that maximizes the area of the corresponding local feasible region \mathcal{Y}_{fa} .

We exploit the computational efficiency of the IP algorithm as in Alg. 2 in order to plan foothold locations that ensure the robot's stability and actuation consistency while traversing rough terrains. As in the previous Section we assume here a static crawl gait with predefined phase durations, where only one foot can break contact at a time. The idea is to find, at each lift-off, the most suitable foothold to maximize the area of the feasible region for the next swing leg. Our strategy consists in sampling a set of p candidate footholds around the *default* target foothold (from heuristics) located along the direction of motion. We then evaluate the height map of the terrain in those sampled points (i.e. correcting the corresponding z coordinate and swing orientation to adapt to the perceived terrain surface⁹) [43], [44]. The default step location is simply a function of the user-defined desired linear and angular velocities of the robot and it neither considers the external map of the surrounding environment, nor the stability and actuation consistency requirements [39].

Fig. 13 shows a foothold planning simulation in which eight different candidate footholds (red balls) are considered.

As additional feature, we discard the footholds that: 1) are close to the edge, 2) would result in a shin collision, 3) are out of the leg's workspace.

In the simulation shown one out of 8 is discarded because it was too close to the edge of the pallet. The next step consists in computing the local feasible regions \mathcal{Y}_{fa}^i for the $p = 8$ considered foot locations ($i = 1, \dots, p$) keeping fixed the set of feet that will be in stance during the following swing phase. Since the local feasible region depends on the robot configuration, we consider the future position of the CoM (computed through the heuristics) for the next triple stance phase and obtain the future joints configuration through inverse kinematics. This joints configuration is then used to update the Jacobians needed for the computation of the candidate local feasible region \mathcal{Y}_{fa}^i . The foothold planner then selects, among the reduced set of admissible footholds, the one that maximizes the area of the corresponding feasible region¹⁰. In the baseline walking on flat terrain, when joint torques are far away from their limits, the default foothold is selected.

⁹To avoid corrections in unwanted directions, we define the sampling direction along the direction of the predicted step, (i.e. in consistency with the desired velocity).

¹⁰Another approach could consist in maximizing the residual radius (i.e. radius of the largest circumference inscribed in the region), however, we noticed that often multiple candidate footholds may return the same residual radius but different areas. This is the case any time that the CoM projection is closer to a friction-related edge of the feasible region rather than an actuation-related edge of the region.

Conversely, on more complex terrain, when the robot is far from a default configuration (e.g. when one leg is much more retracted than the other legs), the scaled version $\hat{\mathcal{Y}}_{fa}$ (described in the previous Section) can take on a small area (see Fig. 13). In this case the default step will be *corrected* (yellow ball in Fig. 13) in order to enlarge this area and, as a consequence, to increase the robustness to model uncertainties and tracking errors. The default target is not visible because, being computed on a planar estimation of the terrain [39], it turns out to be "inside" the pallet.

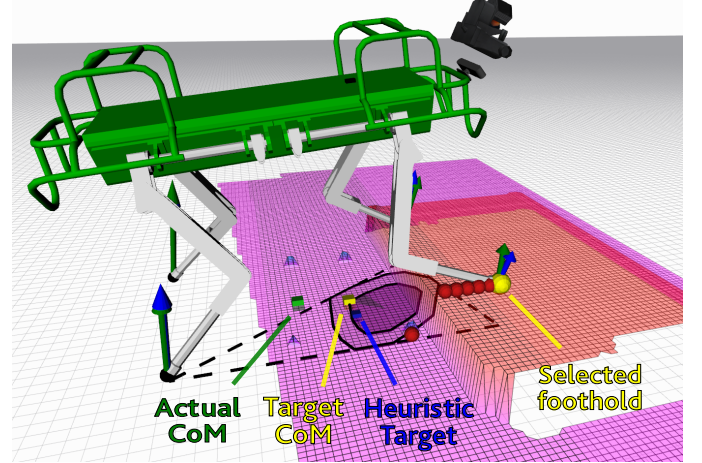


Fig. 13: CoM and foothold planning strategy based on local feasible regions. We show the classical friction region (dashed lines), the feasible region (light gray) and the scaled feasible region (dark gray) with a scaling factor of 0.65. The blue cube is the heuristic target, the yellow one is the CoM target computed from feasible regions, the green one is the actual CoM. The red balls represented the candidate footholds available for the last swing leg. One of the 8 footholds has been discarded because it was too close to the edge. The foothold that has been selected is drawn with a yellow ball.

VI. SIMULATION AND EXPERIMENTAL RESULTS

The superiority of a planning strategy based on the feasible regions with respect to our previous heuristic strategy can be demonstrated by either increasing the load acting on the robot during a standard walk on a flat terrain or by addressing challenging terrains. Both scenarios, and any combination of external loads and complex terrains, take indeed the robot closer to its actuation limits.

As a first result we report the validation of the feasibility margin defined as the distance between the CoM projection and the edges of the feasible region. We then report some simulation and experimental data of the CoM and foothold strategy that we described above in Sec. V-A. The results of this strategy can be seen in the accompanying video¹¹.

A. Validation of the Feasibility Margin

Figure 14 represents the data collected in a simulation where we applied on the CoM of the HyQ robot a vertical increasing load from 0N up to -600N (upper plot). As a consequence of

¹¹https://youtu.be/nmd_8jxtVbU

this external load the feasible region shrinks with a consequent reduction of the feasibility margin r from $0.24m$ to about $0.06m$ (lower plot). Recall that the feasibility margin r is defined as the minimum distance between the CoM projection \mathbf{c}_{xy} and the edges of the feasible region \mathcal{Y}_{fa} (as in (31)). For this validation we also introduce the joint-torque limits violation flag β whose definition is the following:

$$\beta = \begin{cases} 0 & \text{if } \tau_i \in [\tau_i^{max}, \tau_i^{min}], \quad \forall i = 0, \dots, n \\ 1 & \text{otherwise} \end{cases} \quad (34)$$

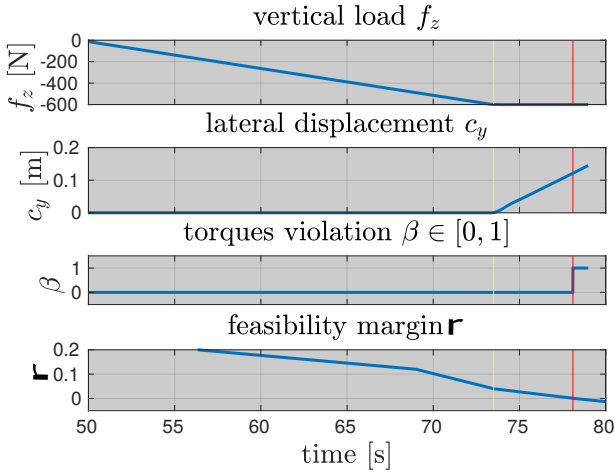


Fig. 14: Validation of the distance between the CoM projection and the edges of the feasible region \mathcal{Y}_{fa} : one of joint-torque limits is hit (*i.e.* $\beta = 1$) approximately at the same time when the feasibility margin r becomes negative (lower plot).

Note that a negative r means that the CoM projection \mathbf{c}_{xy} lies outside the edges of the feasible region \mathcal{Y}_{fa} . After second 74 (yellow vertical line) the external load is fixed to $-600N$ and the robot starts displacing laterally with an increasing c_y coordinate. The second plot from above shows that, when the robot has moved laterally of about $0.12m$ (red vertical line), the feasibility margin r becomes zero and, approximately at the same time, the torque limits violation flag β becomes one, meaning that one of joint-torque limits of the robot has been reached (second plot from below).

B. Walk in Presence of Rough Terrain and External Load

The next simulation result that we report in this Section is a walk over a $22cm$ high pallet, where the HyQ robot only lifts two lateral legs on the pallet while the two other legs always remain on the flat ground. The considerable height of the pallet and the asymmetry of the terrain force the robot to take on complex configurations to step up and down the obstacle and, even if no further external load is applied, the robot might easily reach its joint-torque limits. In this scenario we compare the behavior of two different strategies:

- 1) *friction-region based walk*: this motion planning approach combines the foothold selection strategy explained in Sec. V-B with a CoM motion planning that aims at always keeping the CoM projection inside the scaled friction region $\hat{\mathcal{Y}}_f$;
- 2) *feasible-region based walk*: this approach uses the same foothold strategy as above but makes sure that the CoM

projection always lies inside the scaled feasible region $\hat{\mathcal{Y}}_{fa}$. In this way therefore both friction and actuation constraints are explicitly considered at the motion planning level and are continuously re-planned for.

Evaluating the performance of these two strategies using the feasibility margin r would skew the results in favor of the latter method, considering that it always makes sure that there exists a minimum feasible margin r itself. For the assessment of the two planners' performances we therefore define the minimum joint torque margin r_τ . This corresponds to the minimum distance between the torque of each joint of the robot and their corresponding maximum and minimum values:

$$r_\tau = \min(d_0, \dots, d_n) \quad (35)$$

where:

$$d_i = \min(\tau_i^{max} - \tau_i, \tau_i - \tau_i^{min}), \quad i = 0, \dots, n \quad (36)$$

The quantity r_τ measures how well the proposed online motion planner is able to keep the joint torques away from their limits, while navigating complex geometry environments, being able to reach to the user direction commands or to unexpected disturbances.

It is important to mention that we evaluate r_τ only during the triple support phases (*i.e.* when only three legs are in contact with the ground and the fourth leg is in swing). This is because the triple support phase is the most critical for joint-torque limits (all the robot's weight is loaded on three legs rather than four) and because, as a consequence, the CoM planning strategy optimizes the position of the CoM only for this phase. Because of the static assumption that we assumed in (11), the feasible region computation is only valid when the velocity of the robot's base is zero, condition which is not respected during the four-stance phase (*i.e.* when the robot's base moves).

The values of r_τ for the two simulations are reported in Fig. 15 (above). The red line shows the evolution of r_τ in the case of the friction region-based planning over the entire simulation (up to $14s$). The blue line shows instead the evolution of r_τ in the case of the feasible region-based planning over the entire simulation (up to $21s$). The recording of both simulations is stopped when the robot steps down the pallet with all four legs, the different duration of the simulations is therefore due to the different behavior they present during the negotiation of the pallet. We can notice that the minimum joint torque margin reached by the friction region based simulation of $35Nm$ (dashed red line) occurs towards the conclusion of the experiment when the robot steps down the pallet with the last leg. The feasible region based walk instead performs an increased number of shorter steps before stepping down the pallet, in this way the simulation lasts longer and the minimum joint torque margin of $39Nm$ (dashed blue line) is higher than the simulation where only friction was considered.

The lower plot of Fig. 15 refers instead to a hardware experiment where the HyQ robot walks over a moderately rough terrain made of bricks and plastic tiles while also carrying a $10kg$ extra load on its trunk. Also in this case, as in the simulation, the feasible region based approach presents

a higher minimum joint torque margin of $29Nm$ (dashed blue line) compared to the $21Nm$ margin that we measured for the friction region based approach (dashed red line). The video of the hardware experiments can be found in the accompanying video.

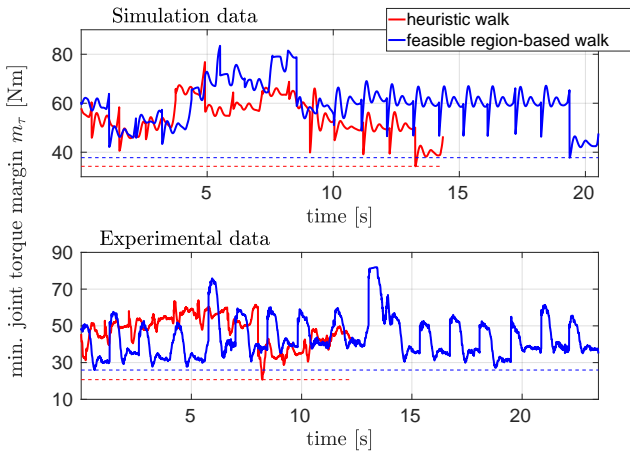


Fig. 15: minimum joint torque margin in simulation and hardware experiments.

VII. CONCLUSION

In this paper we presented a novel approach for projecting joint-torque constraints from the high dimensional joint space ($n + 6$ DoFs) of legged robots to the two-dimensional subspace of the CoM plane orthogonal to gravity. Despite the static assumption and the local nature of the resulting 2D friction- and actuation-consistent regions, this strategy promises to formally improve the robustness of legged robots against frictional stability and against the violation of joint-torque limits. Thanks to the computational efficiency of the local feasible region \mathcal{Y}_{fa} estimation, actuation-consistency and *robustness* can be tested online at a minimum of 50 Hz rate and without any approximation regarding the location and orientation of the contacts. This last point allows our approach to be embedded in a map-based foothold optimization strategy that plans feasible footholds on the height map provided by the vision module (Fig. 13).

We reported experiments both in simulation and on the real platform of the robot crossing a pallet while carrying an external load of $10Kg$. The foothold strategy corrected the steps (*e.g.* making them smaller) when needed to increase the robustness to uncertainty and to disturbances represented by the feasibility margin r .

Modern legged robots are equipped with powerful actuators that are able to sustain the robots own weight even on one single leg in a predefined convenient configuration. Even for such powerful robots, the feasible region can represent a useful tool to intuitively visualize the payload dependency on the specific gait or, finally, the maximal static displacement of the CoM in presence of limited torques and/or damaged limb.

Future works in the same line involve the attempt to compute the feasible region in a closed-form as an alternative to the IP algorithm. Interesting perspectives also involve moving from a sampling-based approach to smooth and continuous gradient-based optimization.

In Sections IV and IV-B we also defined the 2D *global feasible region* \mathcal{G}_{fa} and its 3D counterpart, the *global feasible volume*. While being less computationally efficient than the local actuation region, these can be seen as useful and intuitive tools for the understanding of the dynamic properties of legged robots and their locomotion capabilities, or for long-term offline motion planning. Application examples include, for example, the selection of a feasible robot height in a multi-contact scenario, the CoM planning for a ladder climbing task. As future works we are aiming to extend the descriptiveness of the 2D feasible regions to embed the influence of the robot's trunk orientation and the dynamic effects of inertial accelerations (*e.g.* by relaxing the quasi-static assumption imposed on the wrench polytopes).

The spectrum of possible applications of the 2D actuation-aware regions can be extended also to robotic grasping tasks for the assessment of the grasp feasibility and to industrial manipulators for an intuitive indicator of the dependency between maximal payload and robot configuration.

APPENDIX

We recall in this Appendix few of the main concepts and definitions connected to computational geometry that are heavily used in this manuscript. Most definitions are taken by the following sources [45], [46], [47], [48].

A. Generic Bounded and Unbounded Polyhedra Definitions

Main definitions and terminology used in sets representation and adopted in this paper:

- A convex *polyhedron* \mathcal{H} is a subset of \mathbb{R}^d that solves a finite set of m linear inequalities. The volume of a polyhedron can therefore be either bounded or unbounded. This is a generic definition that may include both (bounded) polytopes and (unbounded) polyhedral cones.

$$\mathcal{H} = \{\mathbf{x} \in \mathbb{R}^d \mid \mathbf{Ax} \leq \mathbf{b}\} \quad (37)$$

with $\mathbf{A} \in \mathbb{R}^{m \times d}$ and $\mathbf{b} \in \mathbb{R}^m$.

- A convex *polytope* \mathcal{P} is a subset of \mathbb{R}^d that solves a finite set of m linear inequalities and is bounded.

$$\mathcal{P} = \{\mathbf{x} \in \mathbb{R}^d \mid \mathbf{Ax} \leq \mathbf{b}\} \quad (38)$$

with $\mathbf{A} \in \mathbb{R}^{m \times d}$ and $\mathbf{b} \in \mathbb{R}^m$.

- A convex *polygon* \mathcal{P} is a polytope in dimension $d = 2$:

$$\mathcal{P} = \{\mathbf{x} \in \mathbb{R}^2 \mid \mathbf{Ax} \leq \mathbf{b}\} \quad (39)$$

with $\mathbf{A} \in \mathbb{R}^{m \times 2}$ and $\mathbf{b} \in \mathbb{R}^m$.

- A convex *zonotope* \mathcal{Z} is a special kind of polytope in \mathbb{R}^d that presents particular symmetry with respect to its center [49], [50]. A zonotope can therefore be fully described by its center $\mathbf{c} \in \mathbb{R}^d$ and its p generators $\mathbf{g} \in \mathbb{R}^d$.

$$\mathcal{Z} = \left\{ \mathbf{c} + \sum_{i=1}^p \alpha_i \mathbf{g}_i \mid \alpha_i \in [-1, 1], \mathbf{g}_i \in \mathbb{R}^d, \mathbf{c} \in \mathbb{R}^d \right\} \quad (40)$$

- A convex *polyhedral cone* \mathcal{C} is a subset of \mathbb{R}^d that solves a finite set of m linear inequalities. Geometrically, each

linear inequality defines a hyperplane that has to pass through the origin.

$$\mathcal{C} = \{\mathbf{x} \in \mathbb{R}^d \mid \mathbf{Cx} \leq \mathbf{0}\} \quad (41)$$

with $\mathbf{A} \in \mathbb{R}^{m \times n}$ and $\mathbf{0} \in \mathbb{R}^m$ is a null vector.

Convex polyhedra, polytopes, zonotopes and cones are called *d*-polyhedra (*d*-polytopes, *d*-zonotopes or *d*-cones) if they have a non-zero interior in \mathbb{R}^d .

In the computational geometry terminology, a hyperplane h of \mathbb{R}^d is a supporting hyperplane of the polyhedron \mathcal{H} if one of the closed halfspaces of h contains \mathcal{H} . A *face* \mathcal{F} of \mathcal{H} is a generic term to indicate either an empty set, \mathcal{H} itself or the intersection between \mathcal{H} and a supporting hyperplane. The *faces* of dimension 0, 1, $d - 1$ and $d - 2$ are usually named *vertices*, *edges*, *ridges* or *facets* [45].

- A *half-space* is either of the two parts in which a hyperplane divides an affine space.
- A *generator* is a broad term to indicate all the elements of Euclidean space \mathbb{R}^d that can be used to represent the considered set. Depending on the considered type of polyhedron, generators may include *vertices*, *rays* (or *edges*).

According to the Minkowski-Weil theorem [47], polyhedra can be equivalently described in terms of their half-spaces (\mathcal{H} -description) or in terms of their generators (\mathcal{G} -, \mathcal{V} -, \mathcal{R} or \mathcal{I} -description). Polytopes, for example, can be equivalently described in terms of \mathcal{H} - and/or \mathcal{V} -description. Polyhedral cones \mathcal{C} can be equivalently described in terms of \mathcal{H} -description (see (41)) and/or \mathcal{R} -description:

$$\mathcal{C} = \left\{ \sum_{i=1}^p \alpha_i \mathbf{r}_i \mid \forall \alpha_i \geq 0, \sum_{i=1}^p \alpha_i = 1, \mathbf{r}_i \in \mathcal{R} \right\} \quad (42)$$

where p is the number of rays of the set of rays \mathcal{R} :

$$\mathcal{R} = \{\mathbf{r}_1, \dots, \mathbf{r}_p \mid \mathbf{r}_i \in \mathbb{R}^d\} \quad (43)$$

A cone, however, can not be represented by \mathcal{V} -description as it only owns one vertex which is placed in the origin of the reference frame.

B. Minkowsky Sums and Convex Cones

In the following we will discuss the main properties of sum of sets and convex hull algorithm:

- Given two convex sets \mathcal{A} and \mathcal{B} , their addition (called *Minkowski sum*), indicated by the operator \oplus , another set is defined as the sum of the all elements of \mathcal{A} with all the elements of \mathcal{B} :

$$\mathcal{A} \oplus \mathcal{B} = \{\mathbf{a} + \mathbf{b} \mid \mathbf{a} \in \mathcal{A}, \mathbf{b} \in \mathcal{B}\} \quad (44)$$

which presents a $\mathcal{O}(a \cdot b)$ time (where a is the cardinality of \mathcal{A} and b is the cardinality of \mathcal{B}).

- For a given convex set $S = \{\mathbf{s}_1, \dots, \mathbf{s}_n \mid \mathbf{s} \in \mathbb{R}^d\}$ composed of n finite elements of dimension d , their *convex hull* is defined as the set of all the convex combinations of all its elements (e.g. the vertices of a polytope):

$$\text{ConvHull}(S) = \left\{ \sum_{i=1}^n \alpha_i \mathbf{s}_i \mid \forall \alpha_i \geq 0, \sum_{i=1}^n \alpha_i = 1 \right\} \quad (45)$$

The convex hull distributes over the Minkowski sum, meaning that the following property holds:

$$\text{ConvHull}(\mathcal{A} \oplus \mathcal{B}) = \text{ConvHull}(\mathcal{A}) \oplus \text{ConvHull}(\mathcal{B}) \quad (46)$$

In the worst-case output the complexity of the problem is $\mathcal{O}(n^{[d/2]})$.

For the computation of many locomotion related geometrical objects, such as the CWC, it is important to notice that, given the \mathcal{R} -representation of two polyhedral cones \mathcal{C}_1 and \mathcal{C}_2 :

$$\begin{aligned} \mathcal{C}_1 &= \left\{ \sum_{i=1}^{p_1} \alpha_i \mathbf{r}_{1,i} \mid \forall \alpha_i \geq 0, \sum_{i=1}^{p_1} \alpha_i = 1, \mathbf{r}_{1,i} \in \mathcal{R}_1 \right\} \\ \mathcal{C}_2 &= \left\{ \sum_{i=1}^{p_2} \alpha_i \mathbf{r}_{2,i} \mid \forall \alpha_i \geq 0, \sum_{i=1}^{p_2} \alpha_i = 1, \mathbf{r}_{2,i} \in \mathcal{R}_2 \right\} \end{aligned} \quad (47)$$

the \mathcal{R} -representation of their Minkowski sum \mathcal{C}_{sum} can be obtained by stacking together (i.e., using the *union* operator \cup) the set of rays \mathcal{R}_1 and \mathcal{R}_2 of the two individual cones:

$$\begin{aligned} \mathcal{C}_{sum} = \mathcal{C}_1 \oplus \mathcal{C}_2 &= \left\{ \sum_{i=1}^{p_1+p_2} \alpha_i \mathbf{r}_i \mid \forall \alpha_i \geq 0, \right. \\ &\quad \left. \sum_{i=1}^{p_1+p_2} \alpha_i = 1, \mathbf{r}_i \in \mathcal{R}_1 \cup \mathcal{R}_2 \right\} \end{aligned} \quad (48)$$

Despite yielding a redundant representation with internal rays, this property allows a considerable speed-up ($\mathcal{O}(p_1 + p_2)$ time) compared to the Minkowski sum of two convex bounded polytopes ($\mathcal{O}(p_1 \cdot p_2)$ time).

REFERENCES

- [1] M. Vukobratović and B. Borovac, "Zero-moment point - thirty five years of its life," *International Journal of Humanoid Robotics*, pp. 157–173, 2004.
- [2] J. Pratt, J. Carff, S. Drakunov, and A. Goswami, "Capture point: A step toward humanoid push recovery," in *IEEE-RAS International Conference on Humanoid Robots*, 01 2007, pp. 200 – 207.
- [3] H.-W. Park, M. Yee, M. Chuah, and S. Kim, "Dynamic Quadruped Bounding Control with Duty Cycle Modulation Using Vertical Impulse Scaling," *IEEE/RSJ International Conference on Intelligent Robots and Systems (IROS)*, 2014.
- [4] R. Orsolino, M. Focchi, D. G. Caldwell, and C. Semini, "A combined limit cycle - zero moment point based approach for omni-directional quadrupedal bounding," *20th International Conference on Climbing and Walking Robots (CLAWAR)*, Porto, Portugal, 2017.
- [5] S. Caron and A. Kheddar, "Dynamic Walking over Rough Terrains by Nonlinear Predictive Control of the Floating-base Inverted Pendulum," in *eprint arXiv:1703.00688*, 2017.
- [6] H. Dai and R. Tedrake, "Planning robust walking motion on uneven terrain via convex optimization," in *Humanoids*, 2016.
- [7] J. Englsberger, C. Ott, and A. Albu-Schäffer, "Three-dimensional biped walking control based on divergent component of motion," *IEEE Transactions on Robotics (TRO)*, vol. 31, 11 2013.
- [8] D. E. Orin, A. Goswami, and S.-H. Lee, "Centroidal dynamics of a humanoid robot," *Auton. Robots*, vol. 35, no. 2-3, pp. 161–176, Oct. 2013. [Online]. Available: <http://dx.doi.org/10.1007/s10514-013-9341-4>
- [9] H. Hirukawa, K. Kaneko, S. Hattori, F. Kanehiro, K. Harada, K. Fujiwara, S. Kajita, and M. Morisawa, "A Universal Stability Criterion of the Foot Contact of Legged Robots - Adios ZMP," in *IEEE International Conference on Robotics and Automation (ICRA)*, 2006.
- [10] T. Saita, Y. Yokokohji, and T. Yoshikawa, "FSW (feasible solution of wrench) for multi-legged robots," in *IEEE International Conference on Robotics and Automation (ICRA)*, 2003. [Online]. Available: <http://ieeexplore.ieee.org/lpdocs/epic03/wrapper.htm?arnumber=1242182>

- [11] A. Del Prete, "Joint position and velocity bounds in discrete-time acceleration/torque control of robot manipulators," *IEEE Robotics and Automation Letters (RA-L)*, vol. 3, no. 1, pp. 281–288, Jan 2018.
- [12] J. Carpentier, R. Budhiraja, and N. Mansard, "Learning Feasibility Constraints for Multi-contact Locomotion of Legged Robots," in *RSS*, 2017.
- [13] J. Carpentier and N. Mansard, "Multi-contact Locomotion of Legged Robots," *IEEE Transactions on Robotics (TRO)*, Aug. 2018. [Online]. Available: <https://hal.laas.fr/hal-01859108>
- [14] P. Fernbach, S. Tonneau, and M. Taix, "Croc: Convex resolution of centroidal dynamics trajectories to provide a feasibility criterion for the multi contact planning problem," in *2018 IEEE/RSJ International Conference on Intelligent Robots and Systems (IROS)*, 2018.
- [15] S. Tonneau, P. Fernbach, A. D. Prete, J. Pettré, and N. Mansard, "2PAC: Two Point Attractors for Center of Mass Trajectories in Multi Contact Scenarios," *ACM Transactions on Graphics (TOG)*, vol. 37, no. 5, p. 176, Jul. 2018. [Online]. Available: <https://hal.archives-ouvertes.fr/hal-01609055>
- [16] R. Orsolino, M. Focchi, C. Mastalli, D. Hongkai, D. G. Caldwell, and C. Semini, "Application of wrench based feasibility analysis to the online trajectory optimization of legged robots," *IEEE Robotics and Automation Letters (RA-L)*, 2018.
- [17] T. Bretl and S. Lall, "Testing static equilibrium for legged robots," *IEEE Transactions on Robotics (TRO)*, vol. 24, no. 4, pp. 794–807, Aug. 2008. [Online]. Available: <http://dx.doi.org/10.1109/TRO.2008.2001360>
- [18] C. Melchiorri, P. Chiacchio, S. Chiaverini, L. Sciavicco, and B. Siciliano, "Comments on "global task space manipulability ellipsoids for multiple-arm systems" and further considerations" [with reply] p. chiacchio, et al," *IEEE Transactions on Robotics and Automation*, vol. 9, no. 2, pp. 232–236, April 1993.
- [19] P. Chiacchio, Y. Bouffard-Vercelli, and F. Pierrot, "Force Polytope and Force Ellipsoid for Redundant Manipulators," *Journal of Robotic Systems*, vol. 14, no. 8, pp. 613–620, 1997. [Online]. Available: [http://doi.wiley.com/10.1002/\(SICI\)1097-4563\(199708\)14:8{3}C613::AID-ROB3{3}E3.0.CO;2-P](http://doi.wiley.com/10.1002/(SICI)1097-4563(199708)14:8{3}C613::AID-ROB3{3}E3.0.CO;2-P)
- [20] P. Chiacchio and M. Concilio, "The dynamic manipulability ellipsoid for redundant manipulators," *IEEE International Conference on Robotics and Automation (ICRA)*, 1998.
- [21] A. L. Cruz Ruiz, S. Caro, P. Cardou, and F. Guay, "ARACHNIS: Analysis of Robots Actuated by Cables with Handy and Neat Interface Software," in *Cable-Driven Parallel Robots, Mechanisms and Machine Science*, vol. 32, 2015, pp. 293 – 305.
- [22] R. Krug, A. J. Lilenthal, D. Kragic, and Y. Bekiroglu, "Analytic Grasp Success Prediction with Tactile Feedback," in *IEEE International Conference on Robotics and Automation (ICRA)*, 2016.
- [23] B. Siciliano, L. Sciavicco, L. Villani, and G. Oriolo, *Robotics: Modelling, Planning and Control*, 1st ed. Springer Publishing Company, Incorporated, 2008.
- [24] B. Siciliano and O. Khatib, *Springer Handbook of Robotics*. Berlin, Heidelberg: Springer-Verlag, 2007.
- [25] P. Chiacchio, S. Chiaverini, L. Sciavicco, and B. Siciliano, "Influence of gravity on the manipulability ellipsoid for robot arms," *Journal of Dynamic Systems Measurement and Control*, vol. 114, pp. 723–727, 12 1992.
- [26] T. Yoshikawa, "Dynamic manipulability of robot manipulators," in *IEEE International Conference on Robotics and Automation (ICRA)*, vol. 2, March 1985, pp. 1033–1038.
- [27] P.-B. Wieber, *Holonomy and Nonholonomy in the Dynamics of Articulated Motion*. Springer Berlin Heidelberg, 07 2006, vol. 340, pp. 411–425.
- [28] V. Samy, S. Caron, K. Bouyarmane, and A. Kheddar, "Post-Impact Adaptive Compliance for Humanoid Falls Using Predictive Control of a Reduced Model," July 2017, eprint hal-01569819.
- [29] C. Boussema, M. J. Powell, G. Bledt, A. J. Ijspeert, P. M. Wensing, and S. Kim, "Online gait transitions and disturbance recovery for legged robots via the feasible impulse set," *IEEE Robotics and Automation Letters (RA-L)*, vol. 4, no. 2, pp. 1611–1618, April 2019.
- [30] J. E. Kelley, "The cutting-plane method for solving convex programs," *Journal of the Society for Industrial and Applied Mathematics*, vol. 8, no. 4, pp. 703–712, 1960. [Online]. Available: <http://www.jstor.org/stable/2099058>
- [31] S. Caron, Q.-C. Pham, and Y. Nakamura, "ZMP support areas for multi-contact mobility under frictional constraints," *IEEE Transactions on Robotics (TRO)*, vol. 33, pp. 67–80, 2017.
- [32] K. Hauser, "Fast interpolation and time-optimization with contact," *The International Journal of Robotics Research*, vol. 33, no. 9, pp. 1231–1250, 2014. [Online]. Available: <http://ijr.sagepub.com/cgi/doi/10.1177/0278364914527855>
- [33] S. Caron and Q.-C. Pham, "When to make a step? tackling the timing problem in multi-contact locomotion by TOPP-MPC," in *2017 IEEE-RAS International Conference on Humanoid Robotics*, Nov. 2017.
- [34] J. C. Trinkle, J.-S. Pang, S. Sudarsky, and G. Lo, "On dynamic multi-rigid-body contact problems with coulomb friction," *ZAMM-Journal of Applied Mathematics and Mechanics/Zeitschrift für Angewandte Mathematik und Mechanik*, vol. 77, no. 4, pp. 267–279, 1997. [Online]. Available: <http://onlinelibrary.wiley.com/doi/10.1002/zamm.19970770411/full>
- [35] A. Del Prete, S. Tonneau, and N. Mansard, "Fast algorithms to test robust static equilibrium for legged robots," in *IEEE International Conference on Robotics and Automation (ICRA)*, 2016.
- [36] M. Eich and T. Vögele, "Design and control of a lightweight magnetic climbing robot for vessel inspection," *19th Mediterranean Conference on Control and Automation*, June 2011.
- [37] R. Hodoshima, T. Doi, Y. Fukuda, S. Hirose, T. Okamoto, and J. Mori, "Development of titan xi: a quadruped walking robot to work on slopes," in *IEEE/RSJ International Conference on Intelligent Robots and Systems (IROS)*, vol. 1, Sept 2004, pp. 792–797 vol.1.
- [38] R. Diankov, "Automated construction of robotic manipulation programs," Ph.D. dissertation, Carnegie Mellon University, Robotics Institute, August 2010. [Online]. Available: http://www.programmingvision.com/rosen_diankov_thesis.pdf
- [39] M. Focchi, R. Orsolino, M. Camurri, V. Barasuol, C. Mastalli, D. G. Caldwell, and C. Semini, "Heuristic Planning for Rough Terrain Locomotion in Presence of External Disturbances and Variable Perception Quality," Nov. 2018, arXiv:11805.10238. [Online]. Available: <https://arxiv.org/pdf/1805.10238.pdf>
- [40] A. Herzog, S. Schaal, and L. Righetti, "Structured contact force optimization for kino-dynamic motion generation," *IEEE/RSJ International Conference on Intelligent Robots and Systems (IROS)*, pp. 2703–2710, 10 2016.
- [41] K. Bouyarmane, K. Chappellet, J. Vaillant, and A. Kheddar, "Quadratic programming for multirobot and task-space force control," *IEEE Transactions on Robotics*, vol. 35, no. 1, pp. 64–77, Feb 2019.
- [42] S. Fahmi, C. Mastalli, M. Focchi, and C. Semini, "Passivity based whole-body control for quadrupedal locomotion on challenging terrain," *ArXiv*, 2018.
- [43] M. Camurri, M. Fallon, S. Bazeille, A. Radulescu, V. Barasuol, D. G. Caldwell, and C. Semini, "Probabilistic contact estimation and impact detection for state estimation of quadruped robots," *IEEE Robotics and Automation Letters*, vol. 2, no. 2, pp. 1023–1030, April 2017.
- [44] S. Nobili, M. Camurri, V. Barasuol, M. Focchi, D. G. Caldwell, C. Semini, and M. Fallon, "Heterogeneous sensor fusion for accurate state estimation of dynamic legged robots," in *Proceedings of Robotics: Science and Systems*, Boston, USA, July 2017.
- [45] K. Fukuda, "Frequently asked questions in polyhedral computation," 1998. [Online]. Available: <https://www.cs.mcgill.ca/~fukuda/soft/polyfaq/polyfaq.html>
- [46] V. Delos and D. Teissandier, "Minkowski sum of HV-polytopes in \mathbb{R}^n ," in *eprint arXiv:1412.2562*, 2014.
- [47] ———, "Minkowski sum of polytopes defined by their vertices," *Journal of Applied Mathematics and Physics*, 2015.
- [48] F. Borrelli, A. Bemporad, and M. Morari, *Predictive Control for Linear and Hybrid Systems*. Cambridge University Press, 2017.
- [49] M. Althoff, "Reachability Analysis and its Application to the Safety Assessment of Autonomous Cars," Ph.D. dissertation, Technische Universität München (TUM), 2010.
- [50] ———, "CORA 2016 Manual," Technische Universität München (TUM), Tech. Rep., 2016.



Romeo Orsolino completed his Bsc. in Mech. Eng. in 2013 and his Msc. in Robotics Eng. in 2015. In the same year, he then joined the DLS team at IIT for a PhD focusing on motion planning for legged locomotion in rough terrains. In February 2019 Romeo successfully defended his PhD thesis titled Actuation-Aware Simplified Dynamic Models for Robotic Legged Locomotion. He is now a post doctoral researcher in the DLS team working motion planning and control, numerical optimization, computational geometry and rigid body dynamics.



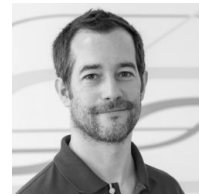
Victor Barasuol was born in So Miguel do Oeste/SC, Brazil. He holds a Diploma in Electrical Engineering from Universidade do Estado de Santa Catarina - UDESC (2006). He has master degree in Electrical Engineering (2008) and a doctorate degree in Automation and Systems Engineering (2013) from Universidade Federal de Santa Catarina - UFSC. Victor Barasuol is currently a senior post-doc researcher of the Dynamic Legged Systems Lab at the Istituto Italiano di Tecnologia - IIT. His main research topics are motion generation and control for quadruped robots with emphases in dynamic locomotion and reactive actions using proprioceptive and exteroceptive sensors.



Michele Focchi is currently a Researcher at the DLS team in IIT. He received both the Bsc. and the Msc. in Control System Engineering from Politecnico di Milano. After gaining some R&D experience in the industry, in 2009 he joined IIT where he developed a micro-turbine for which he obtained an international patent. In 2013, he got a PhD in robotics, getting involved in the Hydraulically Actuated Quadruped Robot project. Currently his research interests are focused on pushing the performances of quadruped robots in traversing unstructured environments, by using optimization-based planning strategies to perform dynamic planning.



Stéphane, Caron is a CNRS researcher at the Laboratoire d'Informatique, de Robotique et de Microélectronique de Montpellier (LIRMM), CNRS-University of Montpellier, France. He received the B.S and M.S. degrees from the École Normale Supérieure of Paris, and the Ph.D. in 2016 from the University of Tokyo, Japan, with a dissertation on multi-contact stability in humanoid motion planning. He was then involved in the H2020 EU project COMANOID, which developed industrial locomotion and manipulation applications of humanoid robots (e.g. factory stair climbing) that were demonstrated on-site at Airbus. His research interests include whole-body control, force control and balance control for legged robots.



Claudio Semini received an Msc. degree in electrical engineering and information technology from ETH Zurich, Switzerland, in 2005. He is currently the Head of the Dynamic Legged Systems (DLS) Laboratory at Instituto Italiano di Tecnologia (IIT). From 2004 to 2006, he first visited the Hirose Laboratory at Tokyo Tech, and later the Toshiba R&D Center, Japan. During his doctorate from 2007 to 2010 at the IIT, he developed the hydraulic quadruped robot HyQ and worked on its control.

After a postdoc with the same department, in 2012, he became the head of the DLS lab. His research interests include the construction and control of versatile, hydraulic legged robots for real-world environments.



Gennaro Raiola received his Bsc. and Msc. degree (magna cumlaude) in computer and automation engineering at the University of Naples Federico II in 2010 and 2012 respectively. He obtained the Ph.D. degree in robotics from the University of Paris-Saclay, France, in February 2017. He worked as research engineer at PAL Robotics and as post doctoral Researcher at the Robotics and Mechatronics group, University of Twente, The Netherlands. Currently he is a Postdoctoral Researcher at the DLS team in IIT. His research interest is focused on software engineering and robotics, in particular on physical human-robot interaction, machine learning applied to controls and inverse kinematics.